ACS OMEGA

Article

Cite This: ACS Omega 2018, 3, 14986−15001

http://pubs.acs.org/journal/acsodf

Structural, Magnetic, and Catalytic Evaluation of Spinel Co, Ni, and Co−Ni Ferrite Nanoparticles Fabricated by Low-Temperature Solution Combustion Process

Jose-Luis Ortiz-Quiñonez,[‡] Umapada Pal,*[,†] and Martin Salazar Villanueva[‡]

[†]Instituto de Física, Benemérita Universidad Autónoma de Puebla, Apartado Postal J-48, 72570 Puebla, Pue., Mexico
[‡]Facultad de Ingeniería, Benemérita Universidad Autónoma de Puebla, Apartado Postal J-39, CP 72570 Puebla, Mexico

Supporting Information

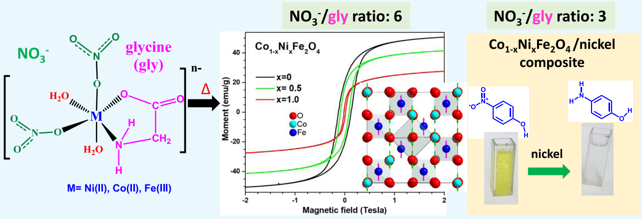

ABSTRACT: Here, we present the low-temperature (~600 °C) solution combustion method for the fabrication of $CoFe_2O_4$, $NiFe_2O_4$, and $Co_{0.5}Ni_{0.5}Fe_2O_4$ nanoparticles (NPs) of 12−64 nm range in pure cubic spinel structure, by adjusting the oxidant (nitrate ions)/reductant (glycine) ratio in the reaction mixture. Although nitrate ions/glycine (N/G) ratios of 3 and 6 were used for the synthesis, phase-pure NPs could be obtained only for the N/G ratio of 6. For the N/G ratio 3, certain amount of Ni^{2+} cations was reduced to metallic nickel. The NH_3 gas generated during the thermal decomposition of the amino acid (glycine, H_2NCH_2COOH) induced the reduction reaction. X-ray diffraction (XRD), Raman spectroscopy, vibrating sample magnetometry, and X-ray photoelectron spectroscopy techniques were utilized to characterize the synthesized materials. XRD analyses of the samples indicate that the $Co_{0.5}Ni_{0.5}Fe_2O_4$ NPs have lattice parameter larger than that of $NiFe_2O_4$, but smaller than that of $CoFe_2O_4$ NPs. Although the saturation magnetization (M_s) of $Co_{0.5}Ni_{0.5}Fe_2O_4$ NPs lies in between the saturation magnetization values of $CoFe_2O_4$ and $NiFe_2O_4$ NPs, high coercivity (H_c, 875 Oe) of the NPs indicate their hard ferromagnetic behavior. Catalytic behavior of the fabricated spinel NPs revealed that the samples containing metallic Ni are active catalysts for the degradation of 4-nitrophenol in aqueous medium.

1. INTRODUCTION

Magnetic nanomaterials are of immense current scientific and technological interest. Although magnetic nanostructures of spinel and rhombohedral perovskite types have shown a great promise to study their unusual magnetic behaviors and associated technological applications, such as high density data storage, memory devices/read-out head,[1−4] they have been routinely applied in the purification of wastewater,[5] bactericide, and organic dye degradation.[6,7] $CoFe_2O_4$ and $NiFe_2O_4$ are interesting ferrimagnetic materials with inverse spinel structure.[3] The reported magnetization values of $CoFe_2O_4$ and $NiFe_2O_4$ nanoparticles (NPs) at 50 000 Oe are generally higher than 60 and 40 emu/g, respectively.[3,8] Nickel ferrite is a soft magnetic material with high electrical resistivity; useful for high-frequency applications, such as transformer cores.[9] The ability to control magnetic properties, such as saturation magnetization, remanent magnetization, and coercivity of these ferrite nanostructures, is important not only for the fundamental understanding of magnetism in these important materials but also for their applications as magnetic resonance imaging contrast-enhancement agents and in magnetic hyperthermia for biomedical therapeutic purposes.[10]

On the other hand, $NiFe_2O_4$ NPs have been utilized in selective oxidation of thiols to produce disulfides (in presence of hydrogen peroxide),[11] cyanation of aryl and heteroaryl halides,[12] reduction of 4-nitrophenol (4-NP) in presence of $NaBH_4$,[13] and gas sensing.[14−16] Most of these applications of $NiFe_2O_4$ NPs are driven by their surface properties, such as presence of (i) metal hydroxides, (ii) remanant organic ligand, and (iii) adsorbed small organic molecules at their surfaces. Therefore, designing and fabricating $NiFe_2O_4$ NPs with tailored surface functionalities are of immense importance for their catalytic applications.[17,18] $NiFe_2O_4$ NPs are also the potential candidates for magnetic separation of gases (i.e., separation of O_2 from air).[19] O_2 is a paramagnetic gas, with relatively high magnetic susceptibility (χ), and can be attracted with magnetizing force produced by the gradient magnetic field. On the other hand, N_2 is diamagnetic gas with low χ.[20]

For the synthesis of metal ferrite nanoparticles, organic solvents,[21] surfactants,[21,22] organometallic compounds,[8] and other organic molecules are often used to control their size and shape.[3,22,23] However, the magnetic properties, such as coercivity (H_c) and saturation magnetization (M_s), of these nanostructures get affected if those organic molecules are not completely removed from the surface of the nanostructures.[24] On the other hand, presence of organic molecules at the

Received: August 30, 2018
Accepted: October 25, 2018
Published: November 6, 2018

DOI: 10.1021/acsomega.8b02229
ACS Omega 2018, 3, 14986−15001

Scheme 1. Stability Constant (β) for the Protonation of the Glycinate Anion Dissolved in Water and Complexation between this Anion with a Nickel(II) Cation in Water

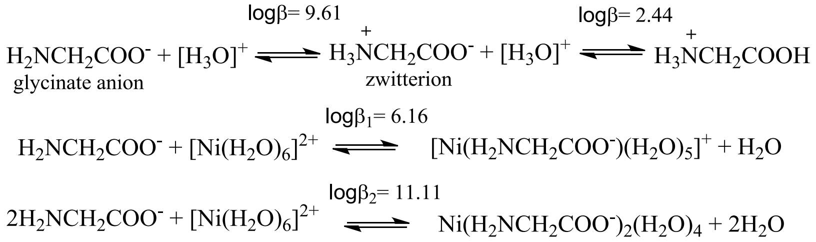

$$\underset{\text{glycinate anion}}{H_2NCH_2COO^-} + [H_3O]^+ \xrightleftharpoons{\log\beta = 9.61} \underset{\text{zwitterion}}{\overset{+}{H_3N}CH_2COO^-} + [H_3O]^+ \xrightleftharpoons{\log\beta = 2.44} \overset{+}{H_3N}CH_2COOH$$

$$H_2NCH_2COO^- + [Ni(H_2O)_6]^{2+} \xrightleftharpoons{\log\beta_1 = 6.16} [Ni(H_2NCH_2COO^-)(H_2O)_5]^+ + H_2O$$

$$2H_2NCH_2COO^- + [Ni(H_2O)_6]^{2+} \xrightleftharpoons{\log\beta_2 = 11.11} Ni(H_2NCH_2COO^-)_2(H_2O)_4 + 2H_2O$$

surface of these nanostructures modifies their catalytic behavior.[24] Common synthesis methods used to fabricate ferrites nanostructures are sol−gel (using citric acid),[25] solvothermal (using ethyleneglycol, sodium acetate, and poly(ethylene glycol)),[3] co-precipitation,[16] and solid-state reaction.[26] Manikandan et al. have reported the synthesis of various ferrite nanoparticles by the microwave combustion method using urea as the fuel.[27] On the other hand, Raju et al.[28] utilized citric acid for the sol−gel syntheses of $CoFe_2O_4$ and $NiFe_2O_4$ nanoparticles, utilizing citrate ions as fuel and as the coordinating agent with metal ions to assist the product formation. A ligand- or surfactant-free aqueous synthesis process generates nanoparticles of organic species-free surfaces, ready for catalysis and sensing.[29] Solution combustion is a method that allows the synthesis of nanoscale materials through mixing metal salts, a fuel (urea, glycine, citric acid, etc.) and an oxidizing agent (HNO_3, NO_3^- ions of the precursor salts, etc.), and a solvent followed by a self-sustained combustion along with a redox reaction.[30] This method usually uses water as solvent, frequently obtaining phase-pure ferrites under optimum experimental conditions. In solution combustion process, organic materials utilized or generated during reaction process are eliminated through high-temperature reactions (including redox reactions) and/or postgrowth thermal annealing under oxygen-rich ambient.

$CoFe_2O_4$ and $NiFe_2O_4$ nanoparticles of unspecified sizes or in bulk form have been fabricated earlier by solution combustion and other methods performing firing at temperatures in between 900 and 1200 °C.[16,26,31] However, high-temperature firing and prolonged annealing produce ferrite nanoparticles of bigger sizes due to temperature-induced growth. To fabricate ferrite nanoparticles of smaller sizes, a low-temperature chemical process or solution combustion at lower firing temperature along with a shorter postgrowth annealing is desirable.

$CoFe_2O_4$ and $NiFe_2O_4$ grow in spinel-type crystal structures, which can be represented by $(Fe^{3+})[Co^{2+}Fe^{3+}]O_4$ and $(Fe^{3+})[Ni^{2+}Fe^{3+}]O_4$, respectively. The cations inside the round brackets are in tetrahedral (A) sites, and the cations inside square brackets are in octahedral (B) sites. The distribution of cations in the crystal lattice depends on several factors, such as the method of preparation, chemical composition, and sintering temperature.[15,28] The distribution of the cations at tetrahedral and octahedral sites modifies the properties of the ferrites. The net magnetization in $CoFe_2O_4$ (or $NiFe_2O_4$) is the difference in the magnetizations of these two (A) and (B) sublattices.[28] As the magnetic contribution of Fe^{3+} cations at (A) sites cancels out the magnetization provided by Fe^{3+} cations at (B) sites, the net magnetization of mixed ferrites, such as $Co_xNi_{1-x}Fe_2O_3$, is governed only by the unpaired spins of the Co^{2+} and Ni^{2+} cations. The number of unpaired spins in the Co^{2+} cation is 3, whereas for the Ni^{2+} cations it is 2. Incorporation of Co^{2+} in $NiFe_2O_4$ produces mixed ferrite $Co_xNi_{1-x}Fe_2O_4$ with both Co^{2+} and Ni^{2+} cations in octahedral (B) sites, producing a small change in the cell parameter of the cubic spinel $NiFe_2O_4$. On the other hand, incorporation of cobalt (Co) in $NiFe_2O_4$ induces increments in (i) the magnetocrystalline anisotropy (and consequently the magnetization) and (ii) the coercivity (H_c) enhancing its application potential in magnetic recording.

A substantial research effort has been devoted by the researchers to fabricate $Co_{0.5}Ni_{0.5}Fe_2O_4$ NPs and their composites.[32,33] For example, Chitra et al. intended to prepare a polyaniline−$Ni_{0.4}Co_{0.6}Fe_2O_4$ nanocomposite by in situ chemical polymerization under ultrasonication, using ferrites NPs prefabricated through a urea-assisted solution combustion process.[34] However, a considerable amount of α-Fe_2O_3 byproduct was formed, as evidenced in their X-ray diffraction (XRD) patterns.[34] On the other hand, Maaz et al.[35] attempted to synthesize $Co_{0.5}Ni_{0.5}Fe_2O_4$ NPs through co-precipitation, obtaining a mixture of Ni- and Co−ferrite, rather than a single homogeneous phase. Magnetic hysteresis loops of the sample with bee-waist type behavior clearly demonstrate the presence of individual ferrite phases.[35] In fact, reports on the fabrication of stoichiometric $Co_{0.5}Ni_{0.5}Fe_2O_4$ NPs in pure spinel phase have been scarce in the literature. $Co_{0.5}Ni_{0.5}Fe_2O_4$ NPs have been fabricated through co-precipitation at solution pH 13, with further annealing at 900 °C for 10 h.[36] Poly(vinyl alcohol)-assisted sol−gel method has also been used to fabricate $Co_{0.5}Ni_{0.5}Fe_2O_4$ NPs. However, the quality of those NPs could not be guessed as their morphological and spectroscopic results were not reported.[37] Therefore, a betterment of conventional methods or implementation of a new technique for the synthesis of stoichiometric, phase-pure spinel ferrites in large scale is of immense current scientific and technological interest.

Although the magnetic properties of spinel cobalt and nickel ferrites have been studied by several research groups,[3,8,13,24,21,38,39] there exist very few reports in the literature on the magnetic properties of $Co_{0.5}Ni_{0.5}Fe_2O_4$ NPs, especially beyond room temperature.[28,36] Furthermore, although Rosnan et al. reported a coercivity field (H_c) of 603.26 Oe for their $Co_{0.5}Ni_{0.5}Fe_2O_4$ NPs fabricated by co-precipitation and postgrowth sintering at 900 °C for 10 h,[36] Raju et al. reported a H_c value of just 250 Oe for their $Co_{0.5}Ni_{0.5}Fe_2O_4$ NPs fabricated by the citrate mediated sol−gel method. As the H_c value is a critical parameter for possible magnetic applications of this ferrite, it is worth to synthesize and study the magnetic properties of $Co_{0.5}Ni_{0.5}Fe_2O_4$ NPs in comparison with phase-pure spinel $CoFe_2O_4$ and $NiFe_2O_4$ NPs fabricated under identical synthesis conditions.

DOI: 10.1021/acsomega.8b02229
ACS Omega 2018, 3, 14986−15001

In this article, we present the fabrication of phase pure, stoichiometric, spinel $CoFe_2O_4$, $NiFe_2O_4$, and $Co_{0.5}Ni_{0.5}Fe_2O_4$ NPs through low-temperature solution combustion process, establishing the role of each of the reagents on the size control of spinel NPs. Effects of Ni incorporation on the magnetic behaviors of the spinel ferrites have been studied over 1.8−350 K. Effects of phase purity and stoichiometry on the catalytic behavior of the metal ferrites have been studied by evaluating their reduction efficiency of 4-nitrophenol, a common organic contaminant in wastewater.

2. RESULTS AND DISCUSSION

2.1. Formation of Ferrites in Solution Combustion Process. The reactions that occur on dissolving glycine in water, together with the stability constant (β) in each step[40] are presented in Scheme 1. The nitric acid added to the aqueous solution induces the protonation of the amine group of the glycinate ligand (also protonation of carboxylate group at pH < 2.44) and shifts the reaction equilibrium to the right. Therefore, the protonation process hampers the bonding of glycinate anion with the Ni(II) cation. It is well known that the glycine forms complexes with transition-metal cations in aqueous solutions.[40] In the presence of hexaaqua complex of nickel(II), the carboxylate group of the glycine first makes a coordinated chemical bond with hexahydrated Ni(II) cation. The ratio between the molar concentrations of the products and the reactants (each concentration must be elevated to its corresponding stoichiometric coefficient) is expressed by the parameter β. For example, β for the second chemical reaction in Scheme 1 can be estimated utilizing the eq 1. The logarithm of the stability constant (β_1) for this reaction is 6.16.[40] The Gibbs energy change for the formation of the Ni−glycinate complex is $\Delta G° = -RT \ln \beta$, where $R = 8.314$ J K^{-1} mol^{-1} and T is the temperature in K. $\Delta G° = -(8.314 \text{ J K}^{-1} \text{ mol}^{-1}) \times (298 \text{ K}) \times (14.18) = -35.1$ kJ per mole of Ni−glycinate complex.

If enough amount of glycine is present in the solution, a second glycinate anion can be bonded to Ni−glycinate complex, generating the $[Ni(H_3NCH_2COO)_2(H_2O)_4]$ complex, for which the logarithm of the stability constant (β_2) is 11.11 (see the third reaction in Scheme 1).[40] If the Ni(II) cations in Scheme 1 are replaced by Co(II) cations, the logarithms of β_1 and β_2 change to 5.10 and 9.10, respectively (see Table 3.4 in ref 40). $\Delta G°$ for the Co(II)−glycinate complex is $-(8.314 \text{ J K}^{-1} \text{ mol}^{-1}) \times (298 \text{ K}) \times (11.74) = -29.1$ kJ/mol. In the chemical equilibria shown in Scheme 1, the higher the value of $\log \beta$, the higher the shift of the equilibrium to the right. Similar compounds can also be formed between glycine anions and hydrated Fe(III) cations. As the values of $\log(\beta_1)$ and $\log(\beta_2)$ are higher for Ni(II)−glycinate complex, in the reactions involving both Ni(II) and Co(II) ions, the glycinate anions form stronger bonding with Ni(II) ions than with Co(II) cations.

$$\beta_1 = \frac{[Ni(H_2NCH_2COO^-)(H_2O)_5{}^+]}{[H_2NCH_2COO^-][Ni(H_2O)_6{}^{2+}]} = 1.445 \times 10^6 \tag{1}$$

Scheme 2 depicts the chelation process between glycine and a Ni(II) cation proposed by Jordan.[41] Although the electronic structure of the glycinate ligand changes once the carboxylate group (COO^-) bonds to the Ni(II) cation, it is difficult for the protonated amine group of the glycinate anion to form bond with the same Ni(II) cation because of low pH used in this work.

Scheme 2. Complexation between Glycinate Anions and a Ni(II) Cation in Water[a]

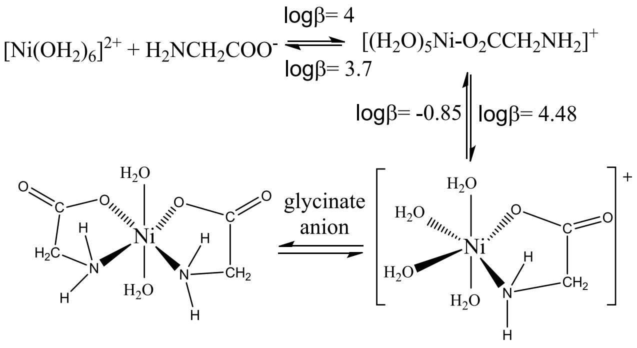

[a] The scheme is adapted from the Scheme 3.10 of ref 41.

2.2. X-ray Diffraction. Figure 1 presents the XRD patterns of the samples synthesized at nitrate ions/glycine (N/G) ratio of 3. As can be noticed, although $CoFe_2O_4$, $NiFe_2O_4$, and $Co_{0.5}Ni_{0.5}Fe_2O_4$ ferrites were formed, metallic nickel and α-Fe_2O_3 byproducts were formed in the samples. Although the formation of metallic nickel in the samples containing Ni precursor is due to the reduction of Ni^{2+} cations by glycine, the formation of α-Fe_2O_3 in all of the samples occurred probably due to the presence of excess iron atoms in the reaction mixture, which did not participate in the formation of $NiFe_2O_4$. The excess of iron atom in the reaction mixture occurs due to the consumption of a fraction of Ni ions to form metallic nickel. Likewise, a very small fraction of cobalt atoms could also be consumed to form metallic cobalt in the mixed oxide, undetected by XRD.

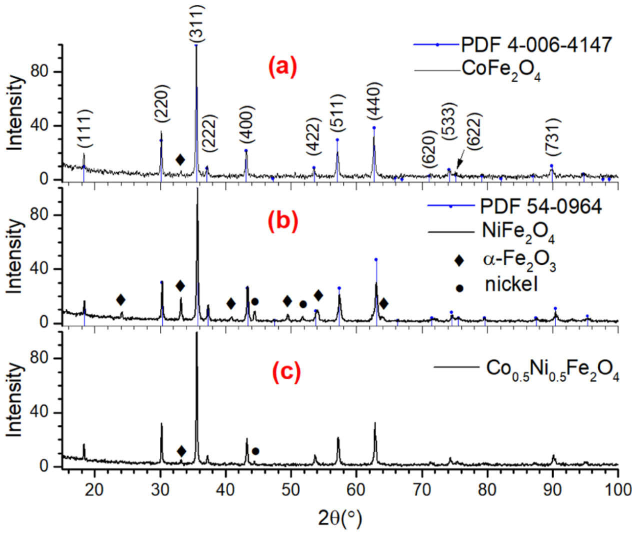

Figure 1. XRD patterns of the (a) $CoFe_2O_4$-3, (b) $NiFe_2O_4$-3, and (c) $Co_{0.5}Ni_{0.5}Fe_2O_4$-3 samples. The diffraction peaks marked with the diamond symbol coincide with the reflections of α-Fe_2O_3 (PDF #04-006-6579). Likewise, the peaks indicated with the filled circles coincide with standard reflections of metallic nickel in cubic phase (PDF #00-004-0850).

As evidenced by the XRD patterns presented in Figure 1, a certain amount of Ni^{2+} cations was also reduced to metallic nickel. As can be perceived from the standard reduction potentials (E^0) of Ni^{2+}, Co^{2+}, Fe^{3+} ions along with nitrate ion and $Ni(glycine)_2$ complex[42] presented in eqs 2−7 of the Scheme 3, the Ni^{2+} cation is easier to reduce than Co^{2+} and Fe^{3+} cations. However, the presence of ligands bonded to metal cations in aqueous media can significantly influence the reduction potential of a metal−ion couple.[43]

Scheme 3. Selected Standard Reduction Potentials that May be Involved in the Formation of Byproduct during the Syntheses of Nickel and Cobalt Ferrites

$$Ni^{2+} + 2e^- \rightleftharpoons Ni(s) \qquad E^0 = -0.236\ V \qquad (2)$$

$$Co^{2+} + 2e^- \rightleftharpoons Co(s) \qquad E^0 = -0.282\ V \qquad (3)$$

$$Fe^{2+} + 2e^- \rightleftharpoons Fe(s) \qquad E^0 = -0.44\ V \qquad (4)$$

$$NO_3^- + 2H^+ + 2e^- \rightleftharpoons 1/2N_2O_4(g) + H_2O \qquad E^0 = 0.798\ V \qquad (5)$$

$$Ni^{2+} + 2glycine^- \rightleftharpoons Ni(glycine)_2 \qquad E^0 = 0.328\ V \qquad (6)$$

$$Ni(glycine)_2 + 2e^- \rightleftharpoons Ni(s) + 2\ glycine^- \qquad E^0 = -0.546\ V \qquad (7)$$

It can also be noted the $Ni(glycine)_2$ complex is harder to be reduced to Ni(s) than Ni^{2+} cations. Moreover, according to the Le Châtelier's principle, addition of higher amount of nitric acid in the reaction mixture will induce protonation of more glycine molecules (see Scheme 1). As the protonated glycine $[H_3NCH_2COOH]^+$ is unable to bond with Ni^{2+} cations, the reaction 6 in Scheme 3 does not occur. Consequently, the Ni^{2+} cations are available to be reduced, as shown in reaction 2. If a fraction of the Ni^{2+} cations is reduced to nickel, or a fraction of Co^{2+} cations is reduced to cobalt, the excess Fe^{3+} cations in the reaction mixture will form α-Fe_2O_3. The process of reduction of Ni^{2+} cations by glycine has been discussed in details in the next paragraphs.According to Li et al.,[44] during the decomposition of glycine at 282 °C, ammonia (NH_3) molecules are formed through a deamination reaction. At 400 °C, the main decomposition products of glycine are HNCO, HCN, and CO. NH_3 is a reducing agent, in which the oxidation state of nitrogen is −3. A thermal decomposition of $Ni(NH_3)_2(H_2NCH_3COO)_2$ complex generates Ni and NiO nanoparticles.[45] Although the formation of diamminediglycinatenickel(II) complexes, such as Ni-$(NH_3)_2(H_2NCH_2COO)_2$, under the reaction conditions used in the present work is quite possible, formation of metallic Ni due to the reduction of Ni^{2+} ion by NH_3 is evident in the XRD patterns presented in Figure 1. An alternative pathway for the formation of metallic Ni in glycine-mediated solution combustion process has also been proposed by Varma et al.,[30] where they assumed the formation of NiO first and then its reduction by NH_3. However, they did not provide the details of involved reactions.

On the other hand, thermal decomposition of hydrated $M(NO_3)_2$ or $M(NO_3)_3$ (M = Co, Ni, and Fe) and HNO_3 generates a mixture of NO_2, N_2O_4, and N_2O_5 gases. These NO_x gases ignite when they get in contact with NH_3 and/or HNCO gases (a hypergolic mixture of gases), generating colorful flame during the ignition,[46] as has been observed for the samples prepared at N/G ratio 3 (see Experimental Section). Higher the amount of glycine in the reaction mixture, higher is the amount of NH_3 or HNCO gas available to produce this flame. Since red-brown gases associated to N_2O_4 (a dimer of NO_2) were not released at the end of the combustion reaction, we can assume that the glycine used in the reaction mixtures completely reduced the NO_3^- ions to colorless N_2 or NO gas. Use of higher amount of glycine in the reaction mixture produces higher amounts of NH_3 or HNCO gas, generating bigger flames during the ignition process. It is worth mentioning that in many cases, when NH_3 molecules are adsorbed on Brønsted acid sites, NH_3 can reduce the toxic NO_x gases to N_2.[45] In addition, the exothermic reaction between NH_3 and HNO_3 (an oxidizing agent) acts as the source of energy required to achieve the self-sustained reaction regime. Such self-sustained reactions were observed to occur in the solution combustion process on utilizing nitrate ions/glycine ratio 3.

To reduce the formation of NH_3 through decomposition of glycine, and consequently to avoid the formation of metallic nickel, the oxidant-agent/reducing-agent (i.e., the N/G) ratio was increased from 3 to 6.

In Figure 2, XRD patterns of the $CoFe_2O_4$ and $NiFe_2O_4$ samples synthesized with N/G ratio 6 are presented. As can be seen in Figure 2 (pattern a), all of the diffraction peaks revealed in the diffraction pattern of $CoFe_2O_4$ sample match perfectly to the standard diffraction pattern (position and

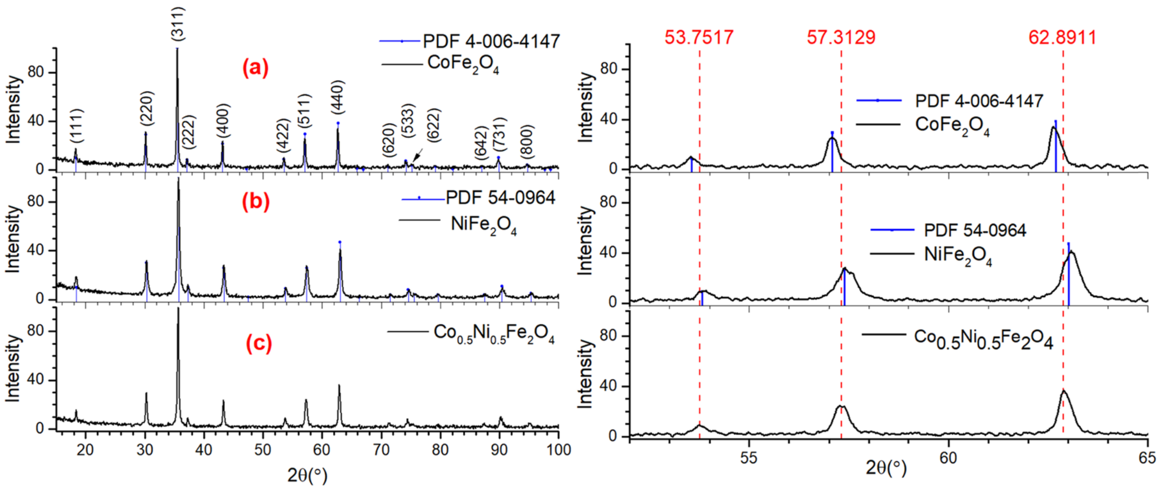

Figure 2. XRD patterns of the (a) $CoFe_2O_4$-6, (b) $NiFe_2O_4$-6, and (c) $Co_{0.5}Ni_{0.5}Fe_2O_4$-6 samples. The same diffractograms zoomed in from 2θ = 52 to 65° are presented in the right panel to show the peak shift with composition variation.

intensity) of spinel $CoFe_2O_4$ (PDF #04-006-4147). Formation of phase-pure $NiFe_2O_4$ spinel nanostructures is also confirmed as the revealed diffraction peaks match both in intensity and in position of peaks in their standard diffraction pattern (PDF #54-0964) (Figure 2, pattern b). Finally, the diffraction pattern of the $Co_{0.5}Ni_{0.5}Fe_2O_4$ sample (Figure 2, pattern c) confirmed the obtention of the ferrite with spinel structure. Apart from the position and intensity matching with standard diffraction pattern, symmetrical shape of all of the diffraction peaks confirms that the ferrite is in single spinel phase. There appeared no additional peak associated to metallic or undesired oxide phase in the diffraction patterns of the samples. However, as can be seen in the right panel of Figure 2, the zoomed-in XRD patterns of all three samples in the 52−65° range, the diffraction peaks of $NiFe_2O_4$ are slightly shifted to higher 2θ values compared with the diffraction peaks of $CoFe_2O_4$. Such a peak shift is very much expected, as the Shannon ionic radius of Ni^{2+} cation (0.55 Å) is slightly smaller than that of Co^{2+} cation (0.58 Å).[47] On the other hand, the diffractogram of the $Co_{0.5}Ni_{0.5}Fe_2O_4$ sample revealed peaks centered around 53.75, 57.31, and 62.89°, which are in between the corresponding peak positions of the $CoFe_2O_4$ and $NiFe_2O_4$ samples, indicating the formation of $Co_{0.5}Ni_{0.5}Fe_2O_4$ phase.

The reported lattice parameters for cubic $CoFe_2O_4$ and $NiFe_2O_4$ are 8.376 Å (PDF #4-006-4147) and 8.337 Å (PDF #54-0964), respectively. However, for $Co_{0.5}Ni_{0.5}Fe_2O_4$, there exist two reported standard lattice parameters: a = 8.3614 Å (PDF #01-083-6066) and a = 8.3468 Å (PDF #00-066-0246).[28,48] These two lattice parameters differ only by 0.0146 Å. The lattice parameters estimated using the (511) and (440) peaks located at 2θ = 57.313 and 62.891° were 8.3465 and 8.3529 Å, respectively, both of which are close to the value reported in the PDF #00-066-0246.

The average crystallite sizes in the $CoFe_2O_4$, $NiFe_2O_4$, and $Co_{0.5}Ni_{0.5}Fe_2O_4$ samples estimated using the Scherrer equation were 52, 25, and 38 nm, respectively, which are in agreement with the peak broadening, evident in the right panel of Figure 2. Therefore, it can be concluded that the N/G ratio in the reaction mixture must be higher than 3 to avoid the formation of metallic nickel and α-Fe_2O_3 byproducts in solution combustion process. As we obtained phase-pure ferrites for N/G ratio 6, the experimental results and associated discussions presented hereafter are only for the samples prepared with N/G ratio of 6.

2.3. Raman Spectroscopy. Figure 3 presents the room-temperature Raman spectra of the spinel ferrite nanostructures. As can be noticed, all of the samples revealed sharp and intense Raman bands indicating their high crystallinity. The Raman spectrum of $CoFe_2O_4$ NPs (Figure 3, trace a) revealed two well-defined intense bands around 473 and 693 cm^{-1} and four lesser intense bands around 207, 307, 570, and 615 cm^{-1}. Although the higher energy bands at 615 and 693 cm^{-1} correspond to the fundamental A_g modes, involving symmetric stretching of oxygen atom with respect to metal−ion in tetrahedral void, frequently observed in crystalline spinel $CoFe_2O_4$ nanostructures,[49] the bands appeared around 207, 307, 473, and 570 cm^{-1} are due to the symmetric and antisymmetric bending of oxygen atom in M−O bond at octahedral voids, corresponding to the $T_{2g}^{(1)}$, E_g, $T_{2g}^{(2)}$, and $T_{2g}^{(3)}$ modes.[49] Cation redistribution in the tetrahedral and octahedral sites in $CoFe_2O_4$ alters the symmetry of the crystal structure from $Fd\bar{3}m$ to $I41/amd$ space group and increases the number of active vibrational modes in Raman spectrum from 5 to 10.[49] That might be the reason for appearing two A_g modes in the Raman spectrum of our $CoFe_2O_4$ NPs (Figure 3a).

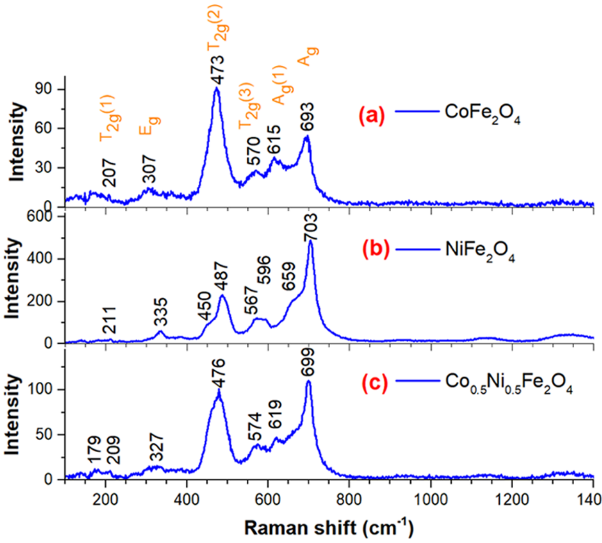

Figure 3. Raman spectra of the $CoFe_2O_4$-6, $NiFe_2O_4$-6, and $Co_{0.5}Ni_{0.5}Fe_2O_4$-6 samples.

On the other hand, the Raman spectrum of $NiFe_2O_4$ sample revealed eight dispersion bands located around 211, 335, 450, 487, 567, 596, 659, and 703 cm^{-1}. The band at 703 cm^{-1} corresponds to the symmetric stretching of oxygen atom with respect to metal−ion in tetrahedral void of spinel $NiFe_2O_4$ lattice. The bands at 211, 335, 487, and 596 cm^{-1} are due to the symmetric and antisymmetric bending of oxygen atom in M−O bond at octahedral voids. Finally, the bands appeared around 450, 567, and 659 cm^{-1} as the shoulders of the intense 487 and 703 Raman bands appeared due to the differences in charge and ionic radii of Ni and Fe ions, producing larger Ni(II)−O bonds in comparison to Fe(III)−O bond,[21] and consequently changing the energy of their bending and stretching vibrations. However, although a same number of dispersion bands appeared in the Raman spectrum of the $Co_{0.5}Ni_{0.5}Fe_2O_4$ sample (Figure 3, trace c), their positions remained in between the positions of corresponding modes in $NiFe_2O_4$ and $CoFe_2O_4$ samples. Although the $T_{2g}^{(2)}$ mode is the most intense Raman band in $CoFe_2O_4$ NPs, the A_g mode is the most intense band in $NiFe_2O_4$ NPs due to its fully symmetric nature. However, the $T_{2g}^{(2)}$ and A_g modes appear with almost same intensity in $Co_{0.5}Ni_{0.5}Fe_2O_4$ due to both nickel and cobalt cations are located at octahedral sites.

2.4. Scanning Electron Microscopy (SEM). Formation of nanometer-sized quasi-spherical particles in the $CoFe_2O_4$, $NiFe_2O_4$, and $Co_{0.5}Ni_{0.5}Fe_2O_4$ samples is very clear in the typical SEM images provided in Figure 4. A simple view of the micrographs can detect the nanoparticles formed in $NiFe_2O_4$ sample are quite smaller than the nanoparticles in $CoFe_2O_4$ sample, and the particles formed in $Ni_{0.5}Co_{0.5}Fe_2O_4$ are of intermediate sizes. The sizes of the particles in the $CoFe_2O_4$, $NiFe_2O_4$, and $Co_{0.5}Ni_{0.5}Fe_2O_4$ samples varied in between 22 and 64 (ca. average size = 39 ± 10 nm), 12 and 42 (ca. average size = 26 ± 8 nm), and 20 and 55 nm (ca. average size = 32 ± 7 nm), respectively. The size variation observed for the samples is in good agreement with their average crystallite sizes determined from XRD spectra (Section 2.2). The size variation of the spinel nanoparticles can be explained considering the

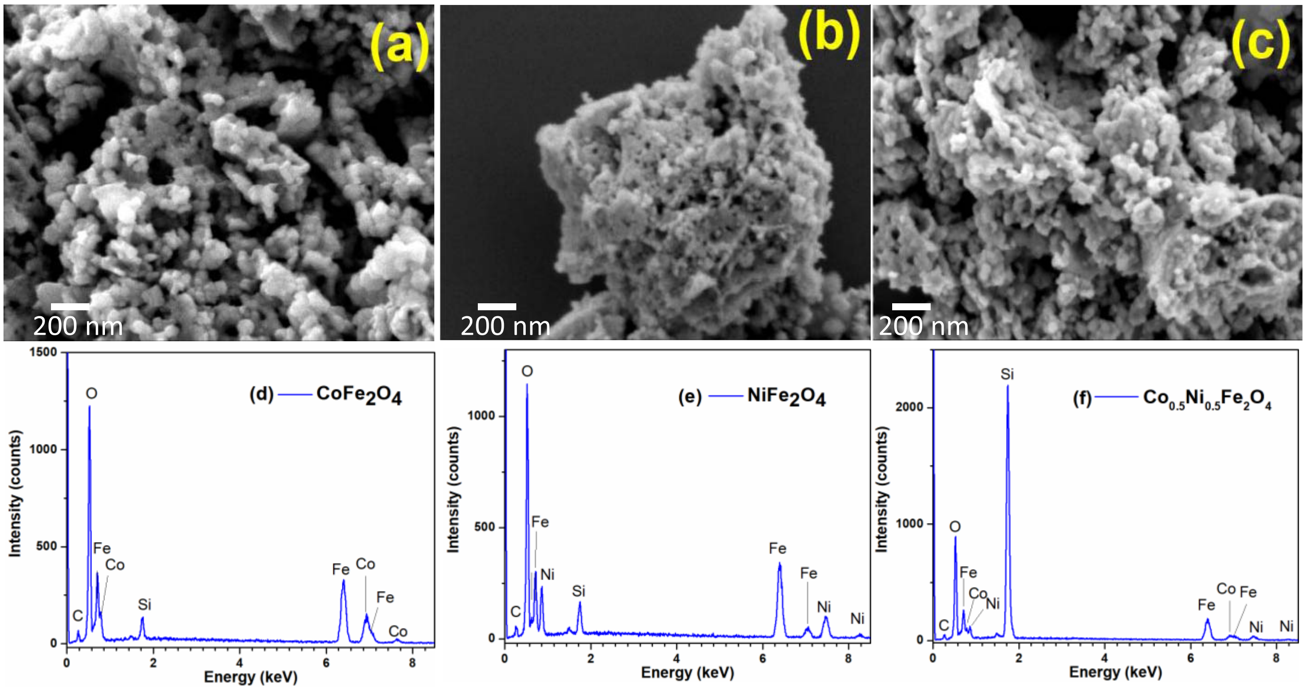

Figure 4. Typical SEM images of the (a) $CoFe_2O_4$-6, (b) $NiFe_2O_4$-6, and (c) $Co_{0.5}Ni_{0.5}Fe_2O_4$-6 nanoparticles. Representative EDS spectra of the samples are presented in (d), (e), and (f), respectively.

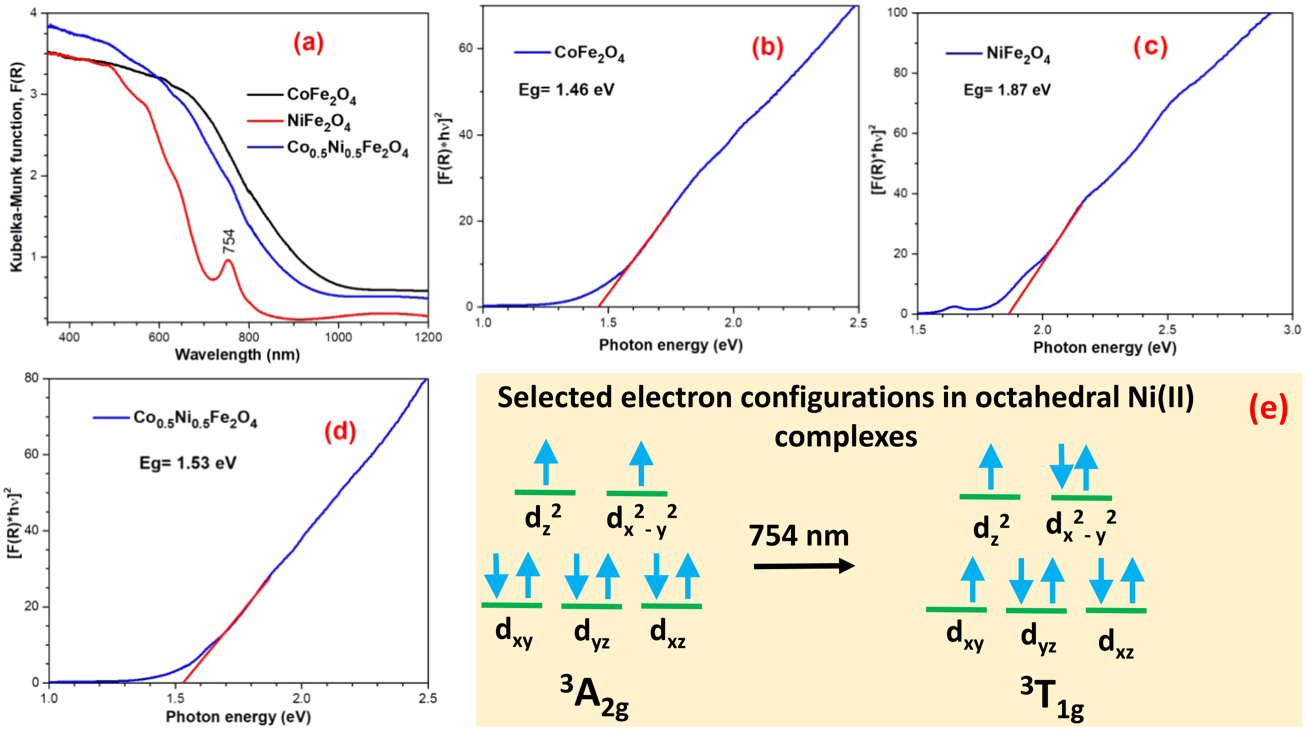

Figure 5. (a) Kubelka–Munk plots (derived from DRS spectra) for the $CoFe_2O_4$-6, $NiFe_2O_4$-6, and $Co_{0.5}Ni_{0.5}Fe_2O_4$-6 NPs and (b–d) their corresponding Tauc' plots to determine their bandgaps. (e) Sketch of the d orbitals in the ground and an excited electron configuration presents in octahedral Ni(II) complexes.[51]

stability constant β of the corresponding metal–glycinate complexes. As has been discussed in Section 2.1, the stability constant of the complex formed between the glycinate anion and the Ni(II) cations is larger ($\beta = 1.445 \times 10^5$) than that of the complex formed between glycinate anion and Co(II) cations ($\beta = 1.259 \times 10^5$). On the other hand, the $\Delta G°$ for these complexes are −35.1 and −29.1 kJ/mol. A more negative $\Delta G°$ value of the complex indicates a higher temperature, and longer annealing time is needed to decompose the complex. Therefore, the $NiFe_2O_4$ NPs were formed at considerably slower growth rate than the $CoFe_2O_4$ NPs at the annealing conditions (600 °C and 2 h) used in the present study. In fact,

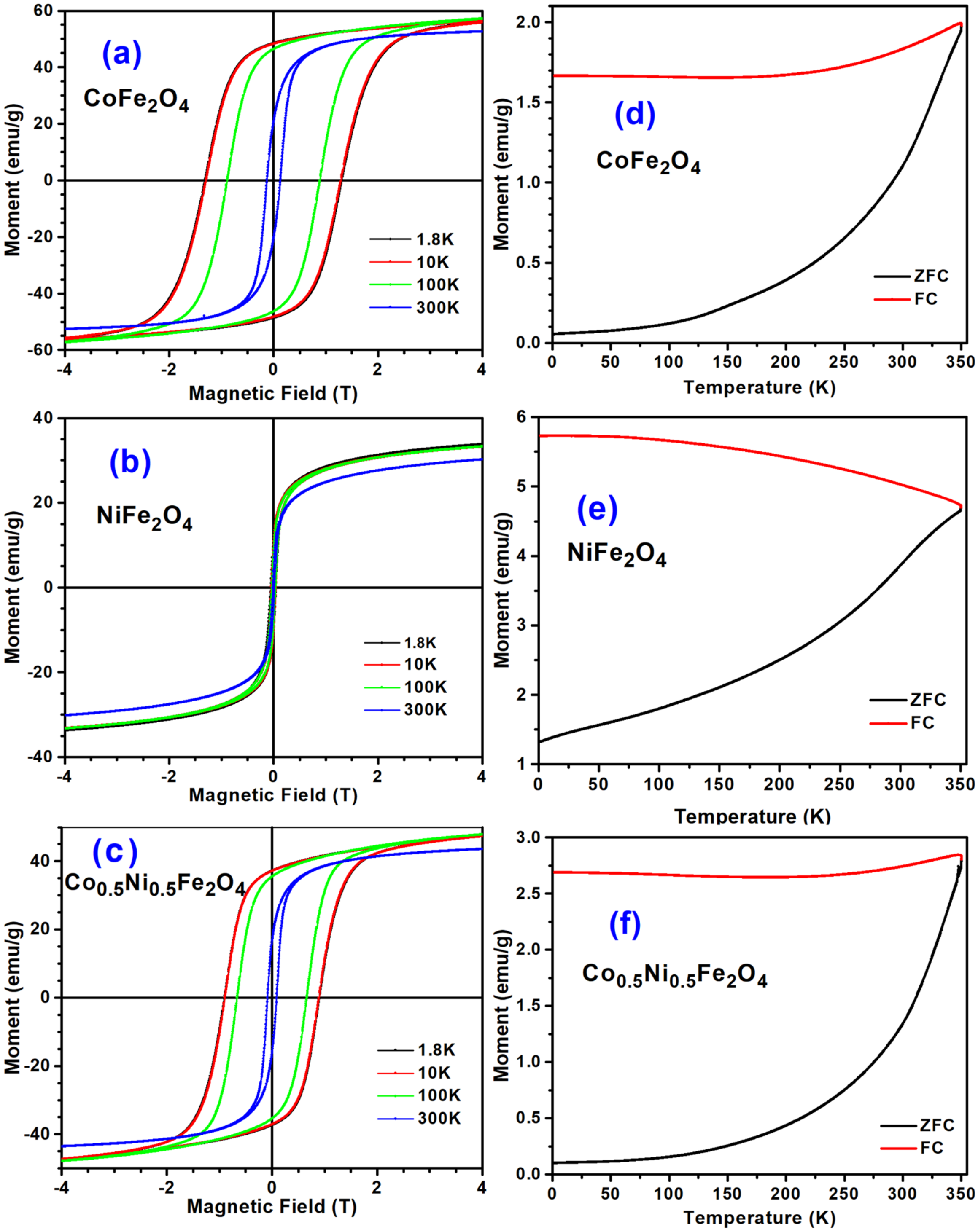

Figure 6. (a, b, c) Magnetization vs applied magnetic field curves at 1.8, 10, 100, and 300 K for CoFe$_2$O$_4$-6, NiFe$_2$O$_4$-6, and Co$_{0.5}$Ni$_{0.5}$Fe$_2$O$_4$-6 NPs. (d, e, f). Zero field cooling (ZFC) and field-cooled (FC) magnetization curves recorded under 200 Oe of applied magnetic field and at 2 K/min for the NPs.

using annealing temperature of 900 °C and 3 h annealing duration, Raju et al. reported to obtain Co$_{0.5}$Ni$_{0.5}$Fe$_2$O$_4$ particles of 100 nm average size, in solution combustion synthesis.[28] The results indicate that the method used in the present work is more convenient for obtaining smaller metal ferrite nanoparticles. Finally, the energy-dispersive X-ray spectroscopy (EDS) (Figure 4d−f) spectra of the samples revealed only the emission peaks of their constituting elements, with no other impurity. The Co/Fe, Ni/Fe, and Co/Ni/Fe atomic ratios estimated by EDS analysis were 1:2, 1:2, and 0.5:0.5:2.0 for (NiFe$_2$O$_4$), (CoFe$_2$O$_4$), and (Co$_{0.5}$Ni$_{0.5}$Fe$_2$O$_4$), respectively.

2.5. Diffuse Reflectance Spectroscopy (DRS). The color of the synthesized CoFe$_2$O$_4$ and Co$_{0.5}$Ni$_{0.5}$Fe$_2$O$_4$ NPs was black, whereas the color of the NiFe$_2$O$_4$ NPs was brown. These colors agree with the position of the absorption edges revealed in the Kubelka−Munk plots of the absorption spectra of ferrite nanostructures presented in Figure 5a. The absorption edge of

Table 1. Magnetic Moment Obtained at $H = 4$ T (M_s), Remanent Magnetization (M_r), and Coercivity Field (H_c) Estimated for the $CoFe_2O_4$, $NiFe_2O_4$, and $Co_{0.5}Ni_{0.5}Fe_2O_4$ NPs Measured at Four Temperatures

sample	temp (K)	M_s (emu/g)	M_r (emu/g)	H_c (Oe)	M_r/M_s
$CoFe_2O_4$	300	52.63	20.87	1274	0.40
	100	57.21	46.499	8862	0.81
	10	56.25	48.367	13 002	0.86
	1.8	56.42	48.367	13 002	0.86
$NiFe_2O_4$	300	30.21	4.00	159	0.13
	100	33.23	8.58	360	0.26
	10	33.27	10.41	422	0.31
	1.8	33.81	9.92	481	0.29
$Co_{0.5}Ni_{0.5}Fe_2O_4$	300	43.56	15.62	886	0.36
	100	47.81	35.40	6591	0.74
	10	47.40	37.16	8955	0.78
	1.8	47.53	37.16	8955	0.78

Table 2. Magnetic Parameters Reported in the Literature at 300 K for $CoFe_2O_4$, $NiFe_2O_4$, and $Co_{0.5}Ni_{0.5}Fe_2O_4$ Nanostructures

	size/length (nm)	shape	M_s (emu/g)	M_r (emu/g)	H_c (Oe)	M_r/M_s	ref
$CoFe_2O_4$	17 ± 0.2	spherical	82.5		~780	0.4	21
	~56	spherical	74.2		930		24
	20	spherical	7.1		9470		24[a]
	180	spherical	60.19		136		3
	39 ± 10	spherical	52.63	20.87	1274	0.40	present work
$NiFe_2O_4$	17 ± 0.2	spherical	62		~10	~0.02	21
	10–25	spherical	40		sp		38
	Ø: 50–60 length: 1000	nanorod	40		40		38
	Ø: 60–65 length: 142–147	nanorod	40.91	13.99	904.46	0.34	8[b]
	24	spherical	44.22	6.74	131.34	0.15	8
	12	spherical	8.5		78		57
	10.9 ± 0.5	cubic	21.32	2	73	0.09	13
	8		25		sp		39
	26 ± 8	spherical	30.21	4.00	159	0.13	present work
$Co_{0.5}Ni_{0.5}Fe_2O_4$	33	spherical	57.35	32.43	603.26	0.57	36
	250–2000		58	8.2	250	0.142	28
	34		56.8		659	0.46	37
	26 ± 7	spherical	43.56	15.62	886	0.36	present work

[a] Oleic acid (0.2 M) capped $CoFe_2O_4$ NPs. [b] Poly(ethylene oxide) was used as a capping agent; sp = superparamagnetic; Ø: diameter.

the $Co_{0.5}Ni_{0.5}Fe_2O_4$ is close to the absorption edge of $CoFe_2O_4$, and although the former contains Ni^{2+} cations, there appeared no absorption band near 754 nm in the absorption spectrum of $Co_{0.5}Ni_{0.5}Fe_2O_4$ (Figure 5a). The bandgaps of the Co and Ni ferrites were estimated through the Tauc' plots (Figure 5b–d). Although the black $CoFe_2O_4$ and $Co_{0.5}Ni_{0.5}Fe_2O_4$ samples revealed direct bandgaps of 1.46 and 1.53 eV, respectively, the brown $NiFe_2O_4$ revealed a direct bandgap of 1.87 eV.

Theoretical band structures for $CoFe_2O_4$ and $NiFe_2O_4$ were reported by Dileep et al.[50] According to the density of states diagram of $CoFe_2O_4$, the electron density at the Fermi level is provided mainly by Co(II) cations in octahedral sites. Likewise, the electron density at the Fermi level of $NiFe_2O_4$ is provided mainly by the Ni(II) cations in octahedral sites. Accordingly, different bandgap values are expected for Co and Ni ferrites. From their calculated band structure for $CoFe_2O_4$, bandgap energies of 0.8 ($X \rightarrow \Gamma$) and 1.6 eV ($\Gamma \rightarrow \Gamma$) were reported.[50] As can be noticed, the calculated energy of the $\Gamma \rightarrow \Gamma$ electronic transition is close to the direct bandgap value (1.46 eV) we determined for $CoFe_2O_4$. On the other hand, bandgap energies of 2.0 ($X \rightarrow \Gamma$) and 2.7 eV ($\Gamma \rightarrow \Gamma$) were obtained from the band structure for $NiFe_2O_4$, which are considerably higher than the bandgap energy (1.87 eV) determined for this ferrite in the present work.

There appeared a sharp absorption band around 754 nm (13263 cm^{-1}) in the absorption spectrum of $NiFe_2O_4$ NPs. Although Liu et al. have also observed the appearance of 754 nm absorption band in the absorption spectrum of $NiFe_2O_4$, its origin was not discussed.[52] Besides, in the electronic absorption spectrum of octahedral Ni(II) complex, a band at 758 nm (13 200 cm^{-1}) was observed by Lancashire and associated to the ${}^3T_{1g} \leftarrow {}^3A_{2g}$ electronic transition.[53] Although the ${}^3A_{2g}$ electron configuration of octahedral Ni(II) complexes designates a nondegenerate state (in which each set of levels is symmetrically occupied), the ${}^3T_{2g}$ electron configuration designates a triply degenerate asymmetrically occupied state (see Figure 5e).[51] The superscript 3 indicates the spin multiplicity due to the two unpaired electrons present in d^8 cations, such as Ni(II). ${}^3A_{2g}$ and ${}^3T_{1g}$ are states representing the ground and an excited energy levels between which an electronic transition occurs both for octahedral Ni(II) complexes and small $NiFe_2O_4$ NPs (Figure 5a,e). This allowed electronic transition, which is also usually represented in the Tanabe–Sugano diagram for cations with d^8 electron configuration.[51]

2.6. Vibrating Sample Magnetometry. The magnetization curves of the $CoFe_2O_4$, $NiFe_2O_4$, and $Co_{0.5}Ni_{0.5}Fe_2O_4$ NPs recorded at different temperatures are presented in Figure 6. It is interesting to note that the hysteresis loops of $CoFe_2O_4$ NPs (Figure 6a) bear typical characteristics of hard ferrimagnetic material, whereas the magnetization curves of $NiFe_2O_4$ NPs (Figure 6b) correspond to very soft ferromagnetic material. The room-temperature coercive field (H_c) of $CoFe_2O_4$ NPs is about 1274 Oe, which increases up to 13 002 Oe at 10 K (Table 2). On the other hand, the isostructural $NiFe_2O_4$ ferrite nanoparticles revealed H_c values at 300 and 10 K of only 158 and 422 Oe, respectively. This difference in the H_c value is due to the smaller anisotropy constant (K_1) for $NiFe_2O_4$. Reported K_1 values for $CoFe_2O_4$ and $NiFe_2O_4$ are 0.27 and −0.0069 MJ/m^3, respectively.[54] K_1 is equal to the energy density necessary to turn the magnetization from the easy to a hard magnetization axis.[54] The simplest expression for the magnetrocrystalline energy is $E_a = K_1 V \sin^2 \theta$, where V stands for the volume of the particle and θ is the angle between the easy and hard magnetization axes.[55] Since the $NiFe_2O_4$ NPs have smaller size (~26 ± 8 nm) and smaller K_1 value than the $CoFe_2O_4$ NPs (~39 ± 10 nm), the H_c value for $NiFe_2O_4$ is considerably smaller than that for $NiFe_2O_4$.

Estimated H_c values (Figure S1) and other magnetic parameters for the $CoFe_2O_4$ and $NiFe_2O_4$ NPs are summarized in Table 1 and compared with some reported values (Table 2). Interestingly, Limaye et al.[24] achieved a huge increase in the H_c values up to 9470 Oe at room temperature by capping their $CoFe_2O_4$ NPs with oleic acid. Such an increase of H_c was attributed to the cumulative effect of surface spin disorder, large strain, and surface anisotropy of the particles due to oleic acid capping.[24] On the other hand, $NiFe_2O_4$ NPs (10 nm) fabricated by Šepelák et al.[56] through high-energy milling process exhibited an H_c value of 2450 Oe (0.245 T) at 4 K. The high H_c value of their $NiFe_2O_4$ NPs was attributed to low degree of inversion ($\lambda = 0.72$) of the cations on (A) and (B) sites in the spinel. Although the H_c value estimated for bulk $NiFe_2O_4$ was very low as all of the Ni^{2+} cations are located in (B) sites, causing a high degree of inversion ($\lambda = 1$), the H_c of their ball-milled $NiFe_2O_4$ NPs decreased substantially after air annealing at 700 °C. Although $NiFe_2O_4$ NPs of about 12 nm average size fabricated by prolonged (30 h) ball-milling process were seen to have coercivity (H_c) around 78 Oe at room temperature,[57] the $NiFe_2O_4$ NPs of about 26 nm average size fabricated in the present study revealed coercivity ~159 Oe at room temperature. Such a discrepancy in the H_c value of the fabricated $NiFe_2O_4$ NPs might be associated to presence of carboxylate groups at their surface, as has been demonstrated from their X-ray photoelectron spectroscopy (XPS) analysis (Section 2.7).

When half of the Co^{2+} cations in $CoFe_2O_4$ is substituted by Ni^{2+} cations, the $(Fe_{1.0}{}^{3+})[Ni_{0.5}{}^{2+}Co_{0.5}{}^{2+}Fe_{1.0}{}^{3+}]$ ferrite is obtained (commonly referred as $Co_{0.5}Ni_{0.5}Fe_2O_4$). In comparison to $CoFe_2O_4$ NPs, the H_c value of the $Co_{0.5}Ni_{0.5}Fe_2O_4$ NPs decreased by ~31% (i.e., up to 886 Oe) and 31.4% (i.e., up to 8962 Oe) at 300 and 10 K, respectively. Obtained hysteresis loops of the $Co_{0.5}Ni_{0.5}Fe_2O_4$ NPs indicate their ferrimagnetic behavior. The coercive field (H_c) of $Co_{0.5}Ni_{0.5}Fe_2O_4$ NPs was seen to depend strongly on their sizes. Although room-temperature H_c values for $Co_{0.5}Ni_{0.5}Fe_2O_4$ NPs of 33 and 34 nm were reported to be 603 and 659 Oe, respectively (Table 2), the reported room-temperature H_c value for larger (200–2000 nm size range) $Co_{0.5}Ni_{0.5}Fe_2O_4$ NPs was only 250 Oe.[28] Higher H_c value obtained in the present study could be due to the presence either of (i) metal hydroxides, (ii) carboxylate groups, and (iii) cations with dangling bonds or all of them at the surface of the $Co_{0.5}Ni_{0.5}Fe_2O_4$ NPs. In fact, due to higher surface area of smaller spinel ferrite NPs in comparison to bigger one, they have higher H_c values, contributed by the earlier mentioned surface species. The presence of metal hydroxides and the carboxylate groups at the surface of these ferrites was confirmed through XPS, as discussed in Section 2.7.

The room-temperature saturation magnetizations (M_s) of the $CoFe_2O_4$ and $NiFe_2O_4$ were only 52.63 and 30.21 emu/g (Figure 6a,b), respectively. The observed lower (~43%) magnetization value of the $NiFe_2O_4$ NPs at room temperature is expected, as the number of unpaired spins in Ni^{2+} cation (two) is lower than the number of unpaired spins in Co^{2+} cation (three). On the other hand, the room-temperature M_s of $Co_{0.5}Ni_{0.5}Fe_2O_4$ NPs was 43.56 emu/g, which is lower than the value (57.12 emu/g) reported by Raju et al.[28] for larger (200–2000 nm) $Co_{0.5}Ni_{0.5}Fe_2O_4$ particles. A variation of room-temperature magnetization with the variation of composition of the ferrite nanoparticles can be seen in Figure 7. The squareness ratio (i.e., M_r/M_s) at 300 K for the $Co_{0.5}Ni_{0.5}Fe_2O_4$ NPs was 0.36, which is close to the ratio obtained for $CoFe_2O_4$ NPs (i.e., 0.40), but larger than for $NiFe_2O_4$ NPs (i.e., 0.13), see Table 1. Since the magnetization curves in Figure 6a,c have a positive slope in between 2 and 4 T, a small paramagnetic contribution is present in the three samples. The paramagnetic contributions in the magnetization curves of the fabricated nanostructures might have come from the cations present at the surface of the NPs.

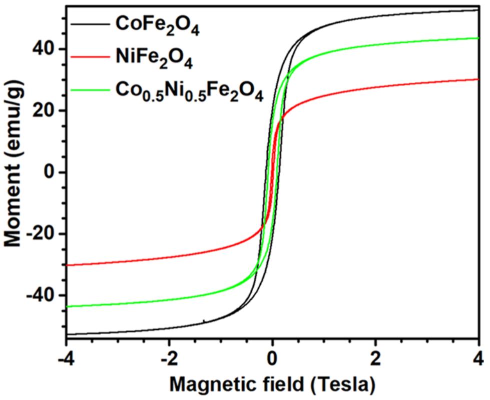

Figure 7. Magnetization vs applied magnetic field curves at 300 K for $CoFe_2O_4$-6, $NiFe_2O_4$-6, and $Co_{0.5}Ni_{0.5}Fe_2O_4$-6.

As can be seen from Figure 6d–f, the zero field cooling (ZFC) curves for the $CoFe_2O_4$ and $Co_{0.5}Ni_{0.5}Fe_2O_4$ NPs are of exponential shape, increasing the magnetic moment with temperature. However, in the case of $NiFe_2O_4$ NPs, the magnetic moment increases almost linearly with temperature in 1.8–220 K range and then increases rather steeply in between 250 and 350 °C, following a quasi-linear behavior. In ZFC scans, a sample is cooled down under zero applied magnetic field. Consequently, at low temperature the net magnetic moment of the sample is low due to random alignment of spins. However, when the sample's temperature is progressively increased, thermal fluctuation of the sample unblocks the frozen spins. These unblocked spins get aligned

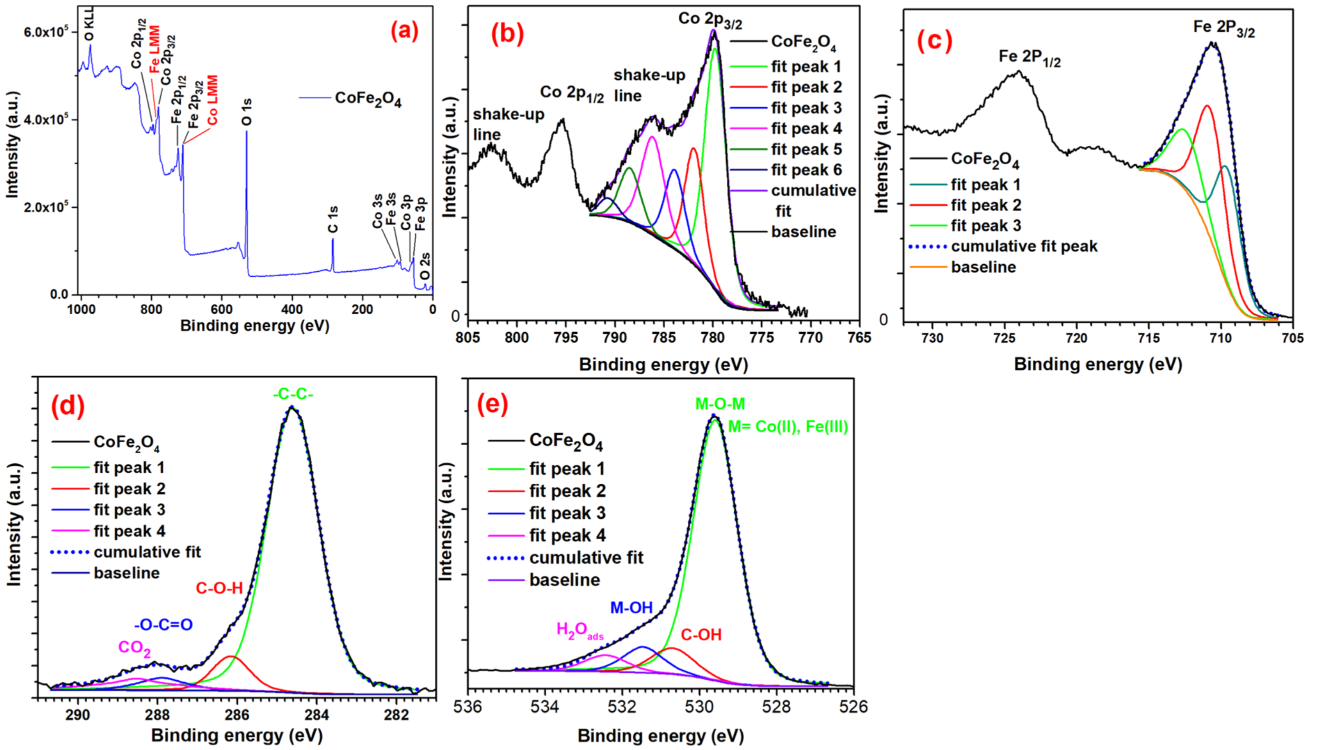

Figure 8. XPS survey spectra of $CoFe_2O_4$-6 NPs (a) and corresponding high-resolution spectra of Co 2p (b), Fe 2p (c), C 1s (d), and O 1s (e) XPS bands. The area and full width at half-maximum (FWHM) of each of the fitted peaks (fit peaks) are presented in Table 3.

Table 3. Binding energy (BE, eV), Full Width at Half-Maximum (FWHM), and Area (%) of the Components of the Representative XPS Emissions for the $CoFe_2O_4$ Sample

	Co $2p_{3/2}$			Fe $2p_{3/2}$			C 1s			O 1s		
peaks	BE	FWHM	area	BE	FWHM	area	BE	FWHM	area	BE	FWHM	area
peak 1	779.7	2.6	40.9	709.5	2.1	35.0	284.6	1.5	84.4	529.6	1.35	80.0
peak 2	781.9	2.3	17.5	710.7	2.3	42.6	286.2	1.1	7.5	530.7	1.33	7.9
peak 3	783.9	2.4	12.5	712.4	2.7	22.4	287.9	1.5	3.4	531.5	1.22	7.1
peak 4	786.1	2.8	17.7				288.5	2.0	4.6	532.4	1.33	4.9
peak 5	788.5	2.5	8.8									
peak 6	790.7	2.3	2.6									

along the applied magnetic field (200 Oe in the present case) increasing the net magnetic moment of the sample (Figure 6d–f). However, neither of the synthesized samples revealed well-defined ZFC maximum, which could be considered as blocking temperature (T_B). Although blocking temperatures of about 350 and 400 K have been reported for $CoFe_2O_4$ and $NiFe_2O_4$ NPs of about 12 and 11 nm average sizes, respectively, in the literature,[13,58] the T_B values for the metal ferrite nanoparticles fabricated in the present study were not possible as they remain above 350 K (beyond the measured temperature range).

On the other hand, the FC curve for the $NiFe_2O_4$ sample revealed a slight decrease in net magnetic moment with the increase of temperature, indicating the alignment of a small fraction of spins under the applied magnetic field (200 Oe) due to a progressive increase in thermal energy (k_BT). This behavior was not observed for the $CoFe_2O_4$ and $Co_{0.5}Ni_{0.5}Fe_2O_4$ samples, probably due to their higher anisotropy constants (K_1) for the cobalt ferrite. The irreversibility temperature, T_{irr} (the temperature at which the ZFC and FC curves of a material get separated), for all of the three ferrites was higher than 350 K, although a T_{irr} of ~40 K has been reported for $NiFe_2O_4$ by Nathani et al.[39]

2.7. X-ray Photoelectron Spectroscopy (XPS). A typical XPS survey spectrum of the $CoFe_2O_4$ sample is depicted in Figure 8a. As expected, only the emissions correspond to cobalt, iron, oxygen, and carbon are revealed in the XPS spectrum. High-resolution XPS spectra for selected atomic orbitals of Co, Fe, C, and O are depicted in Figure 8b–e. The deconvolution of the asymmetric peak associated to the Co $2p_{3/2}$ orbital in the $CoFe_2O_4$ sample generated three component peaks at 779.9, 781.9, and 783.9 eV and its corresponding three shake-up peaks (Figure 8b). The component peak 1 (fit peak 1) corresponds to the Co(II) cations located in the octahedral site (as expected) bonded to oxygen atoms, fit peak 2 at binding energy (BE) of 781.9 eV with smaller area might has generated by the cobalt atoms at the surface of $CoFe_2O_4$ forming Co(II)−hydroxide bonds (Co−OH) and Co(II)−carboxylate bonds (Co−OOC). The fit peak 3 with the smallest area is attributed to $L_3M_{45}M_{45}$ Aüger line of the iron cations.[59] $2p_{1/2}$ and $2p_{3/2}$ orbitals of the cobalt atoms in $CoFe_2O_4$ exhibited satellite peak (also called shake-up lines) at higher energies of the main peaks, which

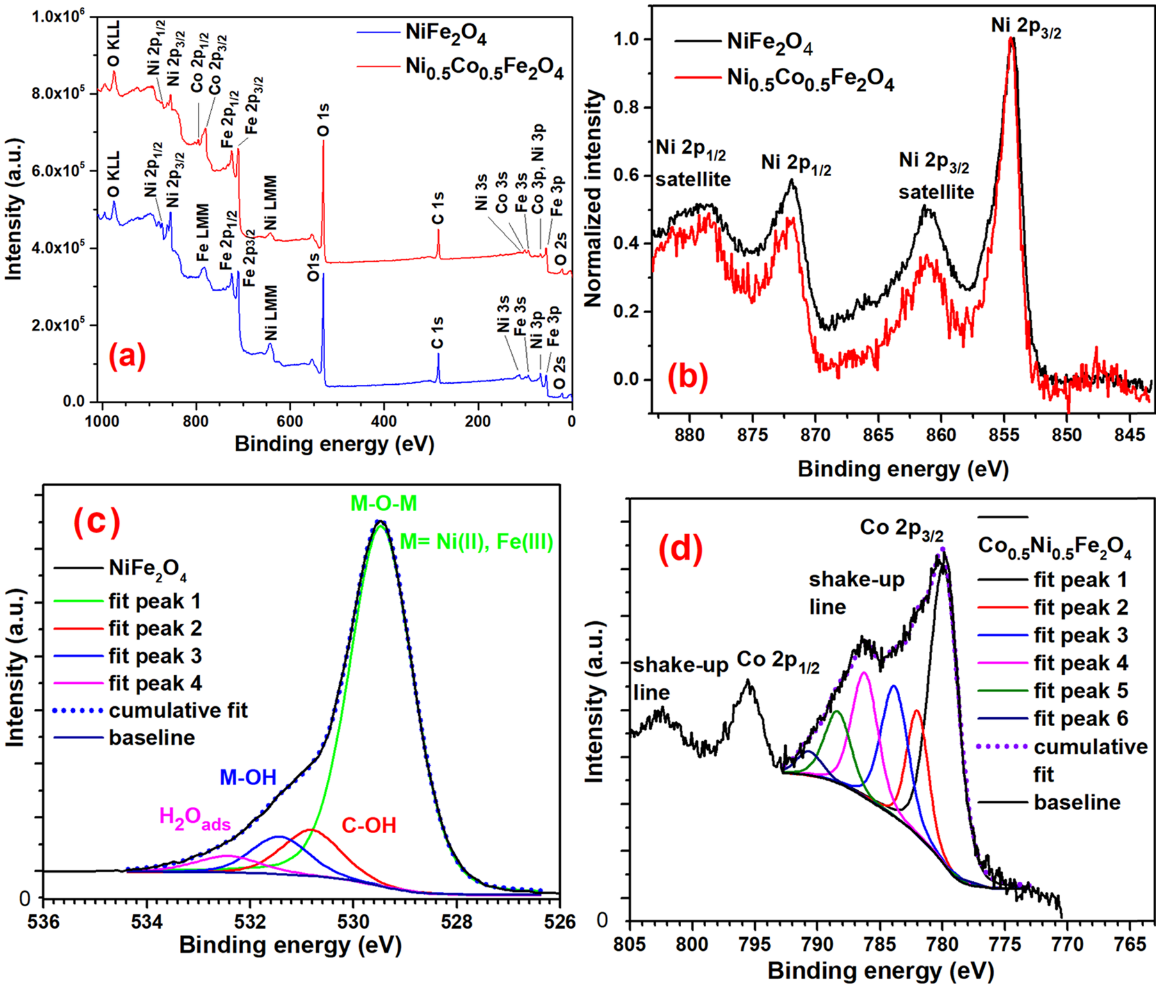

Figure 9. XPS survey spectra of $NiFe_2O_4$-6 and $Co_{0.5}Ni_{0.5}Fe_2O_4$-6 NPs (a) and the high-resolution spectra of selected XPS peaks for one or both of the samples (b–d). The areas of the component (fitted) bands are presented in Table 4.

confirm that the oxidation state of the cobalt cations is 2. (Table 3)

The deconvolution of the Fe $2p_{3/2}$ XPS line for $CoFe_2O_4$ generated three fit peaks located at 709.5, 710.7, and 712.4 eV (Figure 8c). The first and second fit peaks can be attributed to Fe(III) cations located at octahedral and tetrahedral sites, respectively. The fit peak 3, located at BE of 712.4 eV, can be assigned to Fe(III) cations at the surface of the $CoFe_2O_4$ bonded to hydroxyl [OH^-] and carboxylate [COO^-] groups and to the $L_2M_{23}M_{45}$ Aüger line coming from the Co(III) cations.[59] The deconvolution of the C 1s peak confirms the presence of adventitious carbon and suggests the presence of a small amount of molecules with alcohol (7%) and carboxylate (3%) functional groups, adsorbed on the NPs, possibly coming from the decomposition of H_2NCH_2COOH (Figure 8d). Appearance of the component of C 1s peak at 288.5 eV suggests the presence of chemisorbed CO_2.[60] The BE of the 1s orbital of the oxygen atoms in $CoFe_2O_4$ at 529.59 eV is associated to the Co–O and Fe–O chemical bonds in the cobalt ferrite. In addition, there appeared small fit peaks with BE of 530.7, 531.5, and 532.4 eV, indicating the presence of Co–OH, M–OH {M = Co(II), Fe(II)}, and absorbed H_2O at the surface of $CoFe_2O_4$ NPs, respectively (Figure 8e).

XPS survey spectrum of the $NiFe_2O_4$-6 sample shown in Figure 9a indicates that only Ni, Fe, O, and C are present in the sample confirm its purity. XPS peak with BE of 854.4 eV for the Ni $2p_{1/2}$ orbital depicted in Figure 9b confirms the presence of Ni(II)–O chemical bonds in the $NiFe_2O_4$ NPs. Principal component of the O 1s band located at 529.5 eV indicates the presence of Ni(II)–O and Fe(III)–O chemical bonds in the ferrite (Figure 9c and Table 4). Also, the component band with peak position at 531.5 eV indicates the presence of the metal hydroxides {e.g., $Ni(OH)_2$, $Fe(OH)_3$} at the surface of the sample (blue line in Figure 9c).[59] As the shape and position of the XPS peaks for the Fe $2p_{3/2}$ and C 1s orbitals in $NiFe_2O_4$ NPs were very similar to that of the

Table 4. Summary of the Binding Energy (BE, eV), Full Width at Half-Maximum (FWHM), and Area (%) of the Components of the O 1s and Co $2p_{3/2}$ XPS Peaks for the $NiFe_2O_4$ and $Co_{0.5}Ni_{0.5}Fe_2O_4$ Samples

	$NiFe_2O_4$, O 1s			$Co_{0.5}Ni_{0.5}Fe_2O_4$, Co $2p_{3/2}$		
peak number	BE	FWHM	area	BE	FWHM	area
peak 1	529.5	1.45	78.8	779.9	2.72	41.5
peak 2	530.8	1.34	9.5	782.0	2.06	13.2
peak 3	531.4	1.32	7.7	783.8	2.56	17.2
peak 4	532.4	1.56	4.0	786.2	2.48	15.9
peak 5				788.4	2.50	9.2
peak 6				790.7	2.41	3.0

DOI: 10.1021/acsomega.8b02229
ACS Omega 2018, 3, 14986–15001

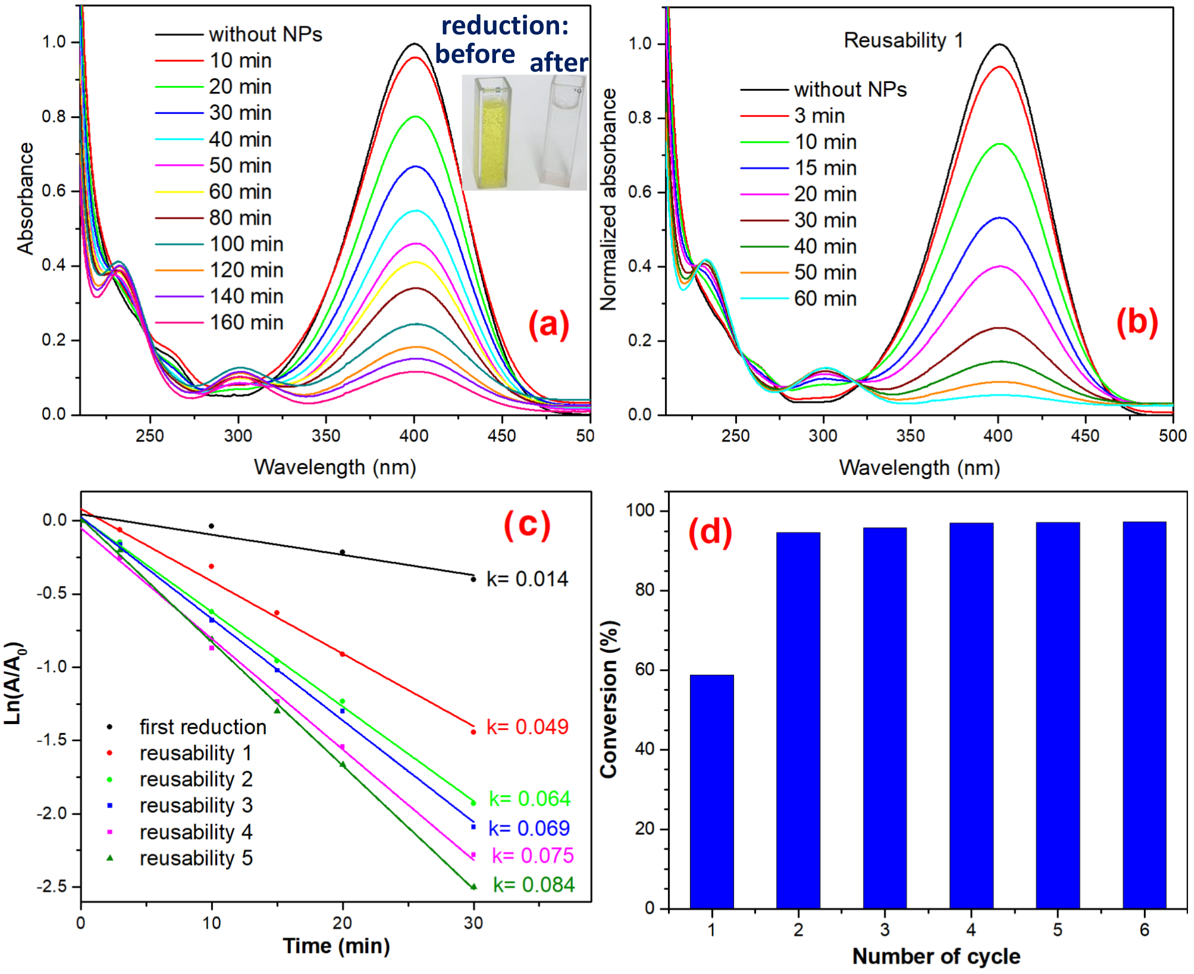

Figure 10. UV–vis absorption spectra correspond to (a) the progressive reduction of 4-nitrophenol to 4-aminophenol using the $NiFe_2O_4$-3 sample as catalyst and (b) the first reusability experiment of the same sample. The time of reaction was counted from the time of addition of the catalyst. (c) Plots of $\ln(A/A_0)$ versus time for the reduction of 4-NP during the first 30 min. (d) Percentage of conversion of 4-NP to 4-AP during the first 60 min.

$CoFe_2O_4$ NPs (Figure S2b and d), they have not been discussed further.(Table 4)

It is evident from Figure S2c (Supporting Information) that the BE of the 1s orbital of the oxygen atoms in $CoFe_2O_4$ is 529.59 eV, whereas for $NiFe_2O_4$ it is 529.46 eV. The difference of these BE values is important because the BE of the O 1s orbital in oxides is correlated to the basicity of these inorganic compounds.[61] In this sense, as O 1s BE decreases, the ability of electron donation by the oxide becomes higher.[62] This electron-donation capability is important to assess the chemical reactivity of the surface of the oxide.

XPS survey spectra of the $Co_{0.5}Ni_{0.5}Fe_2O_4$-6 sample revealed the presence of Co, Ni, Fe, O, and C only in the material (Figure 9a). Deconvolution of the high-resolution XPS band of the Co $2p_{3/2}$ orbital in $Co_{0.5}Ni_{0.5}Fe_2O_4$-6 generated six sub-bands (fit peaks), as observed for the $CoFe_2O_4$ sample. However, as the Figure S2a (Supporting Information) demonstrates, the Co $2p_{3/2}$ peak for the $Co_{0.5}Ni_{0.5}Fe_2O_4$ sample is broader than in the $CoFe_2O_4$ sample. This difference is probably due to the higher nuclear effective charge of the d electrons of the Ni(II) cations (7.5) than for the Co(II) cations (6.9). Since the binding energy of the Co $2p_{3/2}$ orbital is 778 eV and the $L_3M_{23}M_{23}$ Aüger line of nickel is also located at 778 eV,[59] a quantitative estimation of elemental composition for the compound is not possible from its XPS analysis. On the other hand, no major difference in the shape or in the BE in the XPS peaks of Ni 2p orbital for the $Co_{0.5}Ni_{0.5}Fe_2O_4$ and $NiFe_2O_4$ samples was detected (Figure 9b). Since the emission bands for the Fe $2p_{3/2}$, O 1s, and C 1s orbitals in $Co_{0.5}Ni_{0.5}Fe_2O_4$-6 sample are very similar to the corresponding bands for the $CoFe_2O_4$-6 sample (Figure S2b–d, Supporting Information), we did not perform deconvolution of these bands for the $Co_{0.5}Ni_{0.5}Fe_2O_4$-6 samples.

2.8. Catalytic Reduction of 4-Nitrophenol (4-NP) to 4-Aminophenol (4-AP).

Some metallic NPs, such as platinum and silver, have been reported to have catalytic activity in the reduction of 4-NP to 4-AP.[63] However, these chemical elements are expensive. On the other hand, nickel is an earth-abundant element with lower market price and strong ferromagnetic character, which has generated a strong attention as a magnetically separable catalyst for the degradation of organic pollutants.[64] As has been shown in the XRD pattern presented in Figure 1b, the $NiFe_2O_4$-3 sample contains a certain amount of phase-separated nickel NPs. To test the viability of application in catalysis, both the $NiFe_2O_4$-3 and $NiFe_2O_4$-6 samples were tested for the reduction of 4-nitrophenol (4-NP) to 4-aminophenol (4-AP) in their aqueous solution, in presence of a strong reductor sodium borohydride

($NaBH_4$). The details of the experimental procedure adapted for catalytic tests for the ferrites have been presented in Figure S3 (Supporting Information). Although the phase-pure $NiFe_2O_4$-6 sample, with no phase-segregated metallic Ni revealed almost null catalytic activity (results not presented), the phase-impure $NiFe_2O_4$-3 sample with segregated metallic Ni clusters at its surface presented excellent performance in 4-NP reduction. The catalytic activity of the reduction of 4-NP of the sample is summarized in Figure 10a. Although the band located at 400 nm in Figure 10a corresponds to the 4-nitrophenolate ion obtained by the deprotonation of the phenol group on adding $NaBH_4$ in the 4-NP solution, the band appeared around 300 nm is attributed to 4-AP. As can be seen in the inset of Figure 10a and the inset, the $NiFe_2O_4$-3 sample degrades the 4-NP almost fully within 160 min. The reusability of this sample in the catalytic reduction of 4-NP was tested for six cycles by recovering the catalyst from reaction solution magnetically. The kinetic absorption spectra correspond to the second 4-NP degradation cycle for the catalyst are shown in Figure 10b. It is interesting to note that in second cycle of reuse of the catalyst, the reduction of 4-NP is almost 100% within 60 min. In fact, the 4-NP reduction activity of the catalyst remained same in the subsequent four cycles. The results of reusability test of the sample for the cycles 2 to 6 are presented in Figure S4 (Supporting Information).

The difference in the catalytic activity of the sample $NiFe_2O_4$-3 in the first and subsequent reaction cycles can be understood if we consider its fabrication history. The nickel NPs present in the $NiFe_2O_4$-3 sample are responsible for the reduction of 4-NP to 4-AP. However, during the annealing of this sample at 600 °C for 2 h (in air atmosphere), the surface of the nickel NPs probably oxidized to NiO. The NiO shell formed around nickel NPs hinders the charge transfer between the nitrophenolate ion and the nickel NPs. Hence, in the first catalytic cycle, a fraction of the $NaBH_4$ was consumed to reduce the NiO shell to nickel, and consequently the 15 mg of the $NaBH_4$ added was not enough to reduce the 4-NP fully even after 160 min (Figure 10a). In contrast, during the reusability experiments the NiO shell was not present, and a complete reduction of 4-NP to 4-AP (Figure 10b) occurred within 60 min of addition of the catalyst. In fact, the ferrimagnetic $NiFe_2O_4$ NPs act as magnetic support for the smaller superparamagnetic nickel NPs, which are responsible for the catalytic reduction of 4-NP in its aqueous solution. Further, the fabricated phase-pure spinel ferrite nanoparticles of the samples $CoFe_2O_4$-6, $NiFe_2O_4$-6, and $Co_{0.5}Ni_{0.5}Fe_2O_4$-6 have also been tested under same experimental conditions, finding no catalytic activity for the reduction of 4-NP.

Assuming that the reduction reaction follows the Langmuir–Hinshelwood mechanism, with a pseudo first-order kinetics, the expression $\ln(C_t/C_0) = \ln(A_t/A_0) = -kt$ can be used to determine the reaction rate constant (k). C and A stand for the concentration and absorbance of 4-NP at a given time (t), and the subscript 0 stands for the time zero (when $t = 0$). From the $\ln(A_t/A_0)$ versus time plots presented in Figure 10c, it can be seen that the k values for the reusability cycles are around 1.17×10^{-3} s^{-1}. Although the k value for nickel nanowires reported by Sarkar et al. was 3×10^{-2} min^{-1},[65] the k value reported by Zhang et al. for their nickel nanoparticles supported on silica nanotubes is 9.1×10^{-2} s^{-1}.[66]

Nonmagnetic nanoparticles, such as Ag, Pt, Au, Cu, and Pd, commonly used in the reduction of 4-NP, detach away from their supports when they are stirred, and most of the times they cannot be fully recovered from the reaction mixture by filtration.[67] The high catalytic efficiency (~97%) maintained by the $NiFe_2O_4$ NPs fabricated in this work with N/G ratio 3 even after five reusability cycles probably due to the strong magnetic nature of both the catalyst (superparamagnetic nickel clusters) and the support (ferrimagnetic $NiFe_2O_4$ NPs), which not only helps to separate the catalyst from the reaction mixture fully but also reduces the agglomeration of the catalyst (nickel clusters) over the ferrite support.

3. CONCLUSIONS

In summary, we demonstrate a simple solution combustion technique for the fabrication of phase-pure small (26–39 nm average size) $CoFe_2O_4$, $NiFe_2O_4$, and $Co_{0.5}Ni_{0.5}Fe_2O_4$ NPs by adjusting the nitrate/glycine (N/G) ratio to 6 in the reaction mixture. Unlike other synthesis methods utilized to obtain $CoFe_2O_4$ and $NiFe_2O_4$ NPs that use firing temperatures of 900 or 1200 °C and long annealing time, the solution combustion method assisted by glycine requires firing temperatures as low as 600 °C and only 2 h of air annealing. For the N/G ratio 3, a part of the Ni(II) cations and also probably of the Co(II) ions get reduced by glycine to form corresponding metallic nanoparticles, generating α-Fe_2O_3 as a undesired subproduct. Due to lower size, estimated room-temperature saturation magnetization (M_s) values of the fabricated phase-pure (synthesized at N/G ratio 6) spinel ferrite nanostructures are lower than the M_s values reported for the corresponding ferrites in the literature. The room-temperature saturation magnetic moment of the $Co_{0.5}Ni_{0.5}Fe_2O_4$ NPs (43.56 emu/g) remain in between the saturation magnetic moments of $CoFe_2O_4$ NPs (52.63 emu/g) and $NiFe_2O_4$ NPs (30.21 emu/g). Although the room-temperature magnetic coercivity (H_c) of $NiFe_2O_4$ NPs is only 159 Oe, it increases up to 886 Oe when half of the Ni^{2+} cations are replaced by Co^{2+} cations (i.e., for $Co_{0.5}Ni_{0.5}Fe_2O_4$). This H_c value for the $Co_{0.5}Ni_{0.5}Fe_2O_4$ NPs synthesized in this work is 886 Oe, which is even 227 Oe higher than the highest reported H_c value for this material. The observed high H_c value of the $Co_{0.5}Ni_{0.5}Fe_2O_4$ NPs can be attributed to the hydroxyl and carboxylate groups present at the surface of the ferrite. The presence of metal-hydroxides {metal = Co(II), Ni(II), Fe(III)} at the surface of nickel and cobalt ferrites could be detected from their XPS spectra. Although the phase-pure $NiFe_2O_4$, $CoFe_2O_4$, and $Co_{0.5}Ni_{0.5}Fe_2O_4$ NPs fabricated at N/G ratio 6 are not active catalysts, the phase-impure $NiFe_2O_4$ NPs fabricated at the N/G ratio 3 act as highly active catalyst for the degradation of organic pollutant, such as 4-NP. The work presented here demonstrates that it is possible to fabricate phase-controlled, small metal ferrite nanoparticles using a simple solution combustion technique, which can be applied as nonconductive magnetic cores in transformers ($NiFe_2O_4$ NPs). Although the coercivity (886 Oe), saturation magnetization (43.56 emu/g), and remanent magnetization (15.62–43.56 emu/g) values of the fabricated $Co_{0.5}Ni_{0.5}Fe_2O_4$ NPs are very much adequate for their possible application in data storage, the nonstoichiometric $NiFe_2O_4$ NPs (containing Ni clusters) fabricated through N/G ratio-controlled solution combustion process are effective catalysts for 4-nitrophenol degradation.

4. EXPERIMENTAL SECTION

4.1. Reagents and Equipment. The reagents used for the synthesis of ferrite NPs were cobalt nitrate hexahydrate

Table 5. Recipe Used to Prepare Metal Ferrite Nanoparticles at Two Nitrates Ions/Glycine (N/G) Ratios

sample name	$Co(NO_3)_2$ (mmol)	$Ni(NO_3)_3$ (mmol)	$Fe(NO_3)_3$ (mmol)	glycine (mmol)	HNO_3 (mL)	N/G ratio	flame observed	brown gas evolved
$CoFe_2O_4$-3	3		6	12.92	1.0	3.0	yes	no
$NiFe_2O_4$-3		3	6	12.92	1.0	3.0	yes	no
$Co_{0.5}Ni_{0.5}Fe_2O_4$-3	2	2	8	15.59	1.0	3.0	yes	no
$CoFe_2O_4$-6	3		6	5	0.41	6.0	no	yes
$NiFe_2O_4$-6		3	6	5	0.41	6.0	no	yes
$Co_{0.5}Ni_{0.5}Fe_2O_4$-6	2	2	8	6	0.27	6.0	no	yes

($Co(NO_3)_2 \cdot 6H_2O$, Sigma, 99.99%), nickel nitrate hexahydrate ($Ni(NO_3)_2 \cdot 6H_2O$, Sigma, 99.99%), iron nitrate nonahydrate ($Fe(NO_3)_3 \cdot 9H_2O$, Sigma, 99.99%), glycine (H_2NCH_2COOH, Aldrich, 99%), and diluted nitric acid (HNO_3, J.T. Baker, 66%). Powder X-ray diffraction (XRD) patterns of the samples were recorded in a Bruker D8 Discover X-ray diffractometer, providing monochromatic Cu Kα emission (λ = 1.5406 Å) as excitation radiation. Raman spectra of the samples were collected in a LabRAM-HR spectrometer (HORIBA-Jobin Yvon), equipped with a He−Ne laser (λ = 632.8 nm) and a thermoelectrically cooled charged couple device detector. A JEOL JSM-7800F field-emission scanning electron microscope (SEM) operating at 3.0 kV was utilized for morphology and size evaluation of the nanostructures. Magnetization hysteresis loops, zero field cooling (ZFC) and field cooling (FC) curves of the nanostructures were recorded in a physical property measurement system (Dyna Cool-9). Diffuse reflectance spectra (DRS) of the powder samples were recorded in a Varian cary-5000 spectrometer. An X-ray photoelectron spectrometer (XPS, Thermo Scientific) with Al Kα (1486.6 eV) radiation source was utilized to analyze the surface composition of the nanostructures. Deconvolution of the core-level emission bands was performed using Pseudo-Voight2 functions with 70% Gaussian and 30% Lorentzian components, after subtracting Shirley type background.

4.2. Synthesis of Nanoparticles. In a typical synthesis of $CoFe_2O_4$ nanoparticles, 0.873 g of $Co(NO_3)_2 \cdot 6H_2O$, 2.434 g of $Fe(NO_3)_3 \cdot 9H_2O$, and 0.970 g of glycine were dissolved in 70 mL of deionized water in a 600 mL beaker under magnetic stirring. Then, 1 mL of HNO_3 was added to the mixture. The recipes utilized for the synthesis of six samples are provided in Table 5. The prepared mixture solutions were heated at 85 °C (under magnetic stirring) to evaporate the water. On evaporating all of the water from the mixture, an ignition occurred, and in some cases, a flame inside the beaker could be observed (see Table 5). The combustion reaction produced a black or gray powder. It was observed that the flame generated during combustion lasts longer for the samples containing nickel nitrate. The powder samples obtained in the solution combustion process were annealed in an air atmosphere at 600 °C for 2 h, inside a tubular furnace, using a heating ramp of 2 °C/min. The 600 °C temperature was chosen for annealing the fabricated samples, as the temperature was sufficient to eliminate all of the unreacted nitrate precursors and residual carbon from the samples. The annealed samples were grinded in an agata mortar and stored for characterization under nitrogen atmosphere.

The overall chemical reactions occur during the syntheses of $CoFe_2O_4$ and $NiFe_2O_4$ in solution combustion process can be expressed by eqs 8 and 9

$$\begin{aligned} &Co(NO_3)_2(aq) + 2Fe(NO_3)_3(aq) + 2pHNO_3(aq) \\ &\quad + 4nH_2NCH_2COOH(aq) + [9n - 2.5p - 10]O_2 \\ &\quad \rightarrow CoFe_2O_4(s) + (10n + p)H_2O(g) + 8nCO_2(g) \\ &\quad + (2n + p + 4)N_2(g) \end{aligned} \tag{8}$$

$$\begin{aligned} &Ni(NO_3)_2(aq) + 2Fe(NO_3)_3(aq) + 2pHNO_3(aq) \\ &\quad + 4nH_2NCH_2COOH(aq) + [9n - 2.5p - 10]O_2 \\ &\quad \rightarrow NiFe_2O_4(s) + (10n + p)H_2O(g) + 8nCO_2(g) \\ &\quad + (2n + p + 4)N_2(g) \end{aligned} \tag{9}$$

where n and p are the coefficients proportional to the number of utilized moles of nitric acid and glycine, respectively. The coefficients are in accordance with the mass balance of H, N, O, and C in each chemical reaction. Note that if the amount of nitric acid ($2p$) is maintained constant and the amount of glycine ($4n$) is increased, the amount of required O_2 is also increased. However, the CO_2, N_2, and water vapor released during the combustion reaction hamper the entrance of the required O_2 and as a result apart from Ni- and Fe−ferrites, some metallic nickel or cobalt NPs can be generated.

■ ASSOCIATED CONTENT

Ⓢ Supporting Information

The Supporting Information is available free of charge on the ACS Publications website at DOI: 10.1021/acsomega.8b02229.

> Empirical compositions of the samples determined by the EDS technique; selected XPS lines for the $CoFe_2O_4$, $NiFe_2O_4$, and $Co_{0.5}Ni_{0.5}Fe_2O_4$ ferrites; experimental procedure for reduction of 4-nitrophenol (4-NP) to 4-aminophenol; UV−vis spectrum of the reusability experiments of the $NiFe_2O_4$-3.0 sample (PDF)

■ AUTHOR INFORMATION

Corresponding Author

*E-mail: upal@ifuap.buap.mx.

ORCID

Umapada Pal: 0000-0002-5665-106X

Author Contributions

The manuscript was written through contributions of all authors. All authors have given approval to the final version of the manuscript.

Notes

The authors declare no competing financial interest.

■ ACKNOWLEDGMENTS

J.-L.O.-Q. thanks SEP, Mexico, for the postdoctoral fellowship offered through PRODEP grant No. 511-6/17-9449. Partial financial helps offered by the VIEP-BUAP and CONACyT (Grants Nos #100236944-VIEP2018 and INFR-2014-02-23053), Mexíco are acknowledged. The authors acknowledge Dr R. Agustín, CUV-BUAP for his help in acquiring the diffractograms.

■ REFERENCES

(1) Coey, J. M. D. Magnetic Materials. *Magnetism and Magnetic Materials*, 1st ed.; Cambridge University Press: NY, 2009; Vol. *413*, p 423.

(2) Cruz-franco, B.; Gaudisson, T.; Ammar, S.; Bolarín-Miró, A. M.; Jesús, F. S.; De-Mazaleyrat, F.; Nowak, S.; Vázquez-victorio, G.; Ortega-zempoalteca, R.; Valenzuela, R. Magnetic Properties of Nanostructured Spinel Ferrites. *IEEE Trans. Magn.* **2014**, *50*, No. 2800106.

(3) Reddy, M. P.; Mohamed, A. M. A.; Zhou, X. B.; Du, S.; Huang, Q. A Facile Hydrothermal Synthesis, Characterization and Magnetic Properties of Mesoporous $CoFe_2O_4$ Nanospheres. *J. Magn. Magn. Mater.* **2015**, *388*, 40−44.

(4) MacDaniel, T.; Randall, V. Magneto-Optical Thin Film Recording Materials in Practice. *Handbook of Magneto-Optical Data Recording: Materials, Subsystems, Techniques*, 1st ed.; Noyes Publications: Westwood, 1997; p 335.

(5) Zhu, K.; Ju, Y.; Xu, J.; Yang, Z.; Gao, S.; Hou, Y. Magnetic Nanomaterials: Chemical Design, Synthesis, and Potential Applications. *Acc. Chem. Res.* **2018**, *51*, 404−413.

(6) Abraham, A. G.; Manikandan, A.; Manikandan, E.; Vadivel, S.; Jaganathan, S. K.; Baykal, A.; Sri Renganathan, P. Enhanced Magneto-Optical and Photo-Catalytic Properties of Transition Metal Cobalt (Co^{2+} Ions) Doped Spinel $MgFe_2O_4$ Ferrite Nanocomposites. *J. Magn. Magn. Mater.* **2018**, *452*, 380−388.

(7) Teresita, V. M.; Manikandan, A.; Josephine, B. A.; Sujatha, S.; Antony, S. A. Electromagnetic Properties and Humidity-Sensing Studies of Magnetically Recoverable $LaMg_x$ $Fe_{1-x}O_{3-\delta}$ Perovskites Nano-Photocatalysts by Sol-Gel Route. *J. Supercond. Novel Magn.* **2016**, *29*, 1691−1701.

(8) Sivakumar, P.; Ramesh, R.; Ramanand, A.; Ponnusamy, S.; Muthamizhchelvan, C. Synthesis and Characterization of $NiFe_2O_4$ Nanoparticles and Nanorods. *J. Alloys Compd.* **2013**, *563*, 6−11.

(9) Spaldin, N. A. Ferrimagnetism. *Magnetic Material: Fundamentals and Applications*, 2nd ed.; Cambridge University Press: NY, 2010; p 257.

(10) Shirsath, S. E.; Liu, X.; Yasukawa, Y.; Li, S.; Morisako, A. Switching of Magnetic Easy-Axis Using Crystal Orientation for Large Perpendicular Coercivity in $CoFe_2O_4$ Thin Film. *Sci. Rep.* **2016**, *6*, No. 30074.

(11) Kulkarni, A. M.; Desai, U. V.; Pandit, K. S.; Kulkarni, M. A.; Wadgaonkar, P. P. Nickel Ferrite Nanoparticles−hydrogen Peroxide: A Green Catalyst-Oxidant Combination in Chemoselective Oxidation of Thiols to Disulfides and Sulfides to Sulfoxides. *RSC Adv.* **2014**, *4*, 36702−36707.

(12) Matloubi Moghaddam, F.; Tavakoli, G.; Rezvani, H. R. Highly Active Recyclable Heterogeneous Nanonickel Ferrite Catalyst for Cyanation of Aryl and Heteroaryl Halides. *Appl. Organomet. Chem.* **2014**, *28*, 750−755.

(13) Dey, C.; Chaudhuri, A.; Ghosh, A.; Goswami, M. M. Magnetic Cube-Shaped $NiFe_2O_4$ Nanoparticles: An Effective Model Catalyst for Nitro Compound Reduction. *ChemCatChem* **2017**, *9*, 1953−1959.

(14) Patil, J. Y.; Nadargi, D. Y.; Gurav, J. L.; Mulla, I. S.; Suryavanshi, S. S. Synthesis of Glycine Combusted $NiFe_2O_4$ Spinel Ferrite: A Highly Versatile Gas Sensor. *Mater. Lett.* **2014**, *124*, 144−147.

(15) Sivakumar, P.; Ramesh, R.; Ramanand, A.; Ponnusamy, S.; Muthamizhchelvan, C. Preparation and Properties of $NiFe_2O_4$ Nanowires. *Mater. Lett.* **2012**, *66*, 314−317.

(16) Rezlescu, N.; Iftimie, N.; Rezlescu, E.; Doroftei, C.; Popa, P. D. Semiconducting Gas Sensor for Acetone Based on the Fine Grained Nickel Ferrite. *Sens. Actuators, B* **2006**, *114*, 427−432.

(17) Barathiraja, C.; Manikandan, A.; Uduman Mohideen, A. M.; Jayasree, S.; Antony, S. A. Magnetically Recyclable Spinel $Mn_xNi_{1-x}Fe_2O_2$ (X = 0.0−0.5) Nano-Photocatalysts: Structural, Morphological and Opto-Magnetic Properties. *J. Supercond. Novel Magn.* **2016**, *29*, 477−486.

(18) Padmapriya, G.; Manikandan, A.; Krishnasamy, V.; Kumar Jaganathan, S. Spinel $Ni_xZn_{1-x}Fe_2O_4$ ($0.0 \leq x \leq 1.0$) Nano-Photocatalysts: Synthesis, Characterization and Photocatalytic Degradation of Methylene Blue Dye. *J. Mol. Struct.* **2016**, *1119*, 39−47.

(19) Brock, S. L. Aerogels: Disordered, Porous Nanostructures. In *Nanoscale Materials in Chemistry*, 2nd ed.; Klabunde, K. J., Richards, R. S., Eds.; John Wiley & Sons: Hoboken, 2009; pp 225−226.

(20) Madaeni, S. S.; Enayati, E.; Vatanpour, V. Separation of Nitrogen and Oxygen Gases by Polymeric Membrane Embedded with Magnetic Nano-Particle. *Polym. Adv. Technol.* **2011**, *22*, 2556−2563.

(21) Demirci, C. E.; Manna, P. K.; Wroczynskyj, Y.; Akturk, S.; Lierop, J. V. A Comparison of the Magnetism of Cobalt-, Manganese-, and Nickel- Ferrite Nanoparticles. *J. Phys. D: Appl. Phys.* **2018**, *51*, No. 025003.

(22) Lu, A. H.; Salabas, E. L.; Schüth, F. Magnetic Nanoparticles: Synthesis, Protection, Functionalization, and Application. *Angew. Chem., Int. Ed.* **2007**, *46*, 1222−1244.

(23) Mathew, D. S.; Juang, R. S. An Overview of the Structure and Magnetism of Spinel Ferrite Nanoparticles and Their Synthesis in Microemulsions. *Chem. Eng. J.* **2007**, *129*, 51−65.

(24) Limaye, M. V.; Singh, S. B.; Date, S. K.; Kothari, D.; Reddy, V. R.; Gupta, A.; Sathe, V.; Choudhary, R. J.; Kulkarni, S. K. High Coercivity of Oleic Acid Capped $CoFe_2O_4$ Nanoparticles at Room Temperature. *J. Phys. Chem. B* **2009**, *113*, 9070−9076.

(25) Atif, M.; Nadeem, M.; Grössinger, R.; Turtelli, R. S. Studies on the Magnetic, Magnetostrictive and Electrical Properties of Sol-Gel Synthesized Zn Doped Nickel Ferrite. *J. Alloys Compd.* **2011**, *509*, 5720−5724.

(26) Hajalilou, A.; Mazlan, S. A. A Review on Preparation Techniques for Synthesis of Nanocrystalline Soft Magnetic Ferrites and Investigation on the Effects of Microstructure Features on Magnetic Properties. *Appl. Phys. A: Mater. Sci. Process.* **2016**, *122*, No. 680.

(27) Manikandan, A.; Kennedy, L. J.; Bououdina, M.; Vijaya, J. J. Synthesis, Optical and Magnetic Properties of Pure and Co-Doped $ZnFe_2O_4$ Nanoparticles by Microwave Combustion Method. *J. Magn. Magn. Mater.* **2014**, *349*, 249−258.

(28) Raju, K.; Venkataiah, G.; Yoon, D. H. Effect of Zn Substitution on the Structural and Magnetic Properties of Ni-Co Ferrites. *Ceram. Int.* **2014**, *40*, 9337−9344.

(29) Portehault, D.; Delacroix, S.; Gouget, G.; Grosjean, R.; Chan-Chang, T.-H.-C. Beyond the Compositional Threshold of Nanoparticle-Based Materials. *Acc. Chem. Res.* **2018**, *51*, 930−939.

(30) Varma, A.; Mukasyan, A. S.; Rogachev, A. S.; Manukyan, K. V. Solution Combustion Synthesis of Nanoscale Materials. *Chem. Rev.* **2016**, *116*, 14493−14586.

(31) Ahlawat, A.; Sathe, V. G. Raman Study of $NiFe_2O_4$ Nanoparticles, Bulk and Films: Effect of Laser Power. *J. Raman Spectrosc.* **2011**, *42*, 1087−1094.

(32) Babu, K. V.; Sailaja, B.; Jalaiah, K.; Shibeshi, P. T.; Ravi, M. Effect of Zinc Substitution on the Structural, Electrical and Magnetic Properties of Nano-Structured $Ni_{0.5}Co_{0.5}Fe_2O_4$ Ferrites. *Phys. B* **2018**, *534*, 83−89.

(33) De Biasi, R. S.; De Souza Lopes, R. D. Magnetocrystalline Anisotropy of $NiCoFe_2O_4$ Nanoparticles. *Ceram. Int.* **2016**, *42*, 9315−9318.

(34) Chitra, P.; Muthusamy, A.; Jayaprakash, R.; Ranjith Kumar, E. Effect of Ultrasonication on Particle Size and Magnetic Properties of Polyaniline $NiCoFe_2O_4$ Nanocomposites. *J. Magn. Magn. Mater.* **2014**, *366*, 55−63.

(35) Maaz, K.; Karim, S.; Lee, K. J.; Jung, M. H.; Kim, G. H. Effect of Temperature on the Magnetic Characteristics of Ni $_{0.5}$Co$_{0.5}$Fe$_2$O$_4$ Nanoparticles. *Mater. Chem. Phys.* **2012**, *133*, 1006−1010.

(36) Rosnan, R. M.; Othaman, Z.; Hussin, R.; Ati, A. A.; Samavati, A.; Dabagh, S.; Zare, S. Effects of Mg Substitution on the Structural and Magnetic Properties of Co$_{0.5}$Ni$_{0.5\text{-}x}$Mg$_x$Fe$_2$O$_4$ Nanoparticle Ferrites. *Chinese Phys. B* **2016**, *25*, No. 047501.

(37) Niu, Z. P.; Wang, Y.; Li, F. S. Magnetic Properties of Nanocrystalline Co−Ni Ferrite. *J. Mater. Sci.* **2006**, *41*, 5726−5730.

(38) Shan, A.; Wu, X.; Lu, J.; Chen, C.; Wang, R. Phase Formations and Magnetic Properties of Single Crystal Nickel Ferrite (NiFe$_2$O$_4$) with Different Morphologies. *CrystEngComm* **2015**, *17*, 1603−1608.

(39) Nathani, H.; Misra, R. D. K. Surface Effects on the Magnetic Behavior of Nanocrystalline Nickel Ferrites and Nickel Ferrite-Polymer Nanocomposites. *Mater. Sci. Eng., B* **2004**, *113*, 228−235.

(40) Kiss, T.; Sóvágó, I.; Gergely, A. Critical Survey of Stability Constants of Complexes of Glycine. *Pure Appl. Chem.* **1991**, *63*, 597−638.

(41) Jordan, R. B. Ligand Substitution Reactions. In *Reactions Mechanisms of Inorganic and Organometallic Systems*, 3rd ed.; Oxford University Press: NY, 2007; Vol. *80*, p 105.

(42) Harris, D. C. Fundamentals of Electrochemistry. In *Quantitative Chemical Analysis*, 8th ed.; W.H. Freeman and Company: NY, 2010; Vol. *294*, pp AP21−AP24.

(43) Housecroft, C. E.; Sharpe, A. G. Coordination Complexes of the d-Block Metals. *Inorganic Chemistry*; Pearson Education Limited: Harlow, 2012; Vol. *849*−*851*, p 856.

(44) Li, J.; Wang, Z.; Yang, X.; Hu, L.; Liu, Y.; Wang, C. Evaluate the Pyrolysis Pathway of Glycine and Glycylglycine by TG-FTIR. *J. Anal. Appl. Pyrolysis* **2007**, *80*, 247−253.

(45) Centi, G.; Perathoner, S. Selective Catalytic Reduction (SCR) Processes on Metal Oxides. In *Metals Oxides: Chemistry and Applications*, 1st ed.; Fierro, J. L. G., Ed.; CRC Press/Taylor and Francis: Boca Raton, 2006; pp 661−672.

(46) Patil, K. C.; Hegde, M. S.; Rattan, T.; Aruna, S. T. *Chemistry of Nanocrystalline Oxide Materials: Combustion Synthesis, Properties and Applications*; World Scientific Publishing Co.: Singapore, 2008; pp 42−58.

(47) Shannon, R. D. Revised Effective Ionic Radii and Systematic Studies of Interatomie Distances in Halides and Chaleogenides. *Acta Crystallogr., Sect. A* **1976**, *32*, 751−767.

(48) Kumar, A.; Sharma, P.; Varshney, D. Structural, Vibrational and Dielectric Study of Ni Doped Spinel Co Ferrites: Co$_{1-x}$Ni$_x$Fe$_2$O$_4$ (X = 0.0, 0.5, 1.0). *Ceram. Int.* **2014**, *40*, 12855−12860.

(49) Chandramohan, P.; Srinivasan, M. P.; Velmurugan, S.; Narasimhan, S. V. Cation Distribution and Particle Size Effect on Raman Spectrum of CoFe$_2$O$_4$. *J. Solid State Chem.* **2011**, *184*, 89−96.

(50) Dileep, K.; Loukya, B.; Pachauri, N.; Gupta, A.; Datta, R. Probing Optical Band Gaps at the Nanoscale in NiFe$_2$O$_4$ and CoFe$_2$O$_4$ Epitaxial Films by High Resolution Electron Energy Loss Spectroscopy. *J. Appl. Phys.* **2014**, *116*, No. 103505.

(51) Miessler, G. L.; Fisher, P. J.; Tarr, D. A. Coordination Chemistry III: Electronic Spectra. In *Inorganic Chemistry*, 5th ed.; Pearson Education, Inc.: Boston, 2014; pp 417−428.

(52) Liu, Y.; Song, Y.; You, Y.; Fu, X.; Wen, J.; Zheng, X. NiFe$_2$O$_4$/g-C$_3$N$_4$ Heterojunction Composite with Enhanced Visible-Light Photocatalytic Activity. *J. Saudi Chem. Soc.* **2018**, *22*, 439−448.

(53) Lancashire, R. Tanabe-Sugano Diagrams. http://wwwchem.uwimona.edu.jm/courses/Tanabe-Sugano/TSHelp.html (accessed Jun 4, 2018).

(54) Sellmyer, D.; Skomski, R. *Advanced Magnetic Nanostructures*, 1st ed.; Springer: NY, 2006; pp 494.

(55) Skomski, R.; Zhou, J. Nanomagnetic Models. In *Advanced Magnetic Nanostructures*; Sellmyer, D., Skomski, R., Eds.; Springer: NY, 2006; p 52.

(56) Šepelák, V.; Bergmann, I.; Kipp, S.; Becker, K. D. Nanocrystalline Ferrites Prepared by Mechanical Activation and Mechanosynthesis. *Z. Anorg. Allg. Chem.* **2005**, *631*, 993−1003.

(57) Hajalilou, A.; Hashim, M.; Ebrahimi-Kahrizsangi, R.; Mohamed Kamari, H.; Sarami, N. Synthesis and Structural Characterization of Nano-Sized Nickel Ferrite Obtained by Mechanochemical Process. *Ceram. Int.* **2014**, *40*, 5881−5887.

(58) Song, Q.; Zhang, Z. J. Shape Control and Associated Magnetic Properties of Spinel Cobalt Ferrite Nanocrystals. *J. Am. Chem. Soc.* **2004**, *126*, 6164−6168.

(59) Moulder, J. F.; Stickle, W. F.; Sobol, P. F.; Kenneth, B. D. *Handbook of X-ray Photoelectron Spectroscopy*, 1st ed.; Perkin-Elmer Corporation: Eden Prairie, 1992; Vol. *44*, pp 80−85.

(60) Favaro, M.; Xiao, H.; Cheng, T.; Goddard, W. A.; Yano, J.; Crumlin, E. J. Subsurface Oxide Plays a Critical Role in CO$_2$ Activation by Cu(111) Surfaces to Form Chemisorbed CO$_2$, the First Step in Reduction of CO$_2$. *Proc. Natl. Acad. Sci. U.S.A.* **2017**, *114*, 6706−6711.

(61) Busca, G. Acid and Basic Catalysts: Fundamentals. In *Heterogeneous Catalytic Materials: Solid State Chemistry, Surface Chemistry and Catalytic Behaviour*; Elsevier: Amsterdam, 2014; pp 57−93.

(62) Ono, Y.; Hattori, H. Preparation and Catalytic Properties of Solid Base Catalysts—II. Specific Materials for Solid Bases. In *Solid Base Catalysis*, 1st ed.; Springer-Verlag: Berlin, 2011; pp 157−218.

(63) Aditya, T.; Pal, A.; Pal, T. Nitroarene Reduction: A Trusted Model Reaction to Test Nanoparticle Catalyst. *Chem. Commun.* **2013**, *1*−*3*, 1−20.

(64) Kalwar, N. K.; Sirajuddin; Soomro, R. A.; Sherazi, S. T. H.; Hallam, K. R.; Khaskheli, A. R. Synthesis and Characterizations of Highly Efficient Nickel Nanocatalysts and Their Use in Ultra Fast Catalytic Degradation of Organic Dyes. *Int. J. Met.* **2014**, *2014*, No. 126103.

(65) Sarkar, S.; Sinha, A. K.; Pradhan, M.; Basu, M.; Negishi, Y.; Pal, T. Redox Transmetalation of Prickly Nickel Nanowires for Morphology Controlled Hierarchical Synthesis of Nickel/Gold Nanostructures for Enhanced Catalytic Activity and SERS Responsive Functional Material. *J. Phys. Chem. C* **2011**, *115*, 1659−1673.

(66) Dong, Z.; Le, X.; Dong, C.; Zhang, W.; Li, X.; Ma, J. Ni@Pd Core-Shell Nanoparticles Modified Fibrous Silica Nanospheres as Highly Efficient and Recoverable Catalyst for Reduction of 4-Nitrophenol and Hydrodechlorination of 4-Chlorophenol. *Appl. Catal., B* **2015**, *162*, 372−380.

(67) Feng, J.; Fan, D.; Wang, Q.; Ma, L.; Wei, W.; Xie, J.; Zhu, J. Facile Synthesis Silver Nanoparticles on Different Xerogel Supports as Highly Efficient Catalysts for the Reduction of P-Nitrophenol. *Colloids Surf., A* **2017**, *520*, 743−756.